The Astrophysical Journal, 965:155 (23pp), 2024 April 20 https://doi.org/10.3847/1538-4357/ad2455

Secondary Whistler and Ion-cyclotron Instabilities Driven by Mirror Modes in Galaxy Clusters

Francisco Ley[1], Ellen G. Zweibel[1,2], Drake Miller[1], and Mario Riquelme[3]
[1] Department of Astronomy, University of Wisconsin-Madison, Madison, WI 53706, USA
[2] Department of Physics, University of Wisconsin-Madison, 1150 University Avenue, Madison, WI 53706, USA
[3] Departamento de Física, Facultad de Ciencias Físicas y Matemáticas, Universidad de Chile, Chile
Received 2023 September 27; revised 2024 January 29; accepted 2024 January 29; published 2024 April 16

Abstract

Electron cyclotron waves (whistlers) are commonly observed in plasmas near Earth and the solar wind. In the presence of nonlinear mirror modes, bursts of whistlers, usually called lion roars, have been observed within low magnetic field regions associated with these modes. In the intracluster medium (ICM) of galaxy clusters, the excitation of the mirror instability is expected, but it is not yet clear whether electron and ion cyclotron (IC) waves can also be present under conditions where gas pressure dominates over magnetic pressure (high β). In this work, we perform fully kinetic particle-in-cell simulations of a plasma subject to a continuous amplification of the mean magnetic field $\boldsymbol{B}(t)$ to study the nonlinear stages of the mirror instability and the ensuing excitation of whistler and IC waves under ICM conditions. Once mirror modes reach nonlinear amplitudes, both whistler and IC waves start to emerge simultaneously, with subdominant amplitudes, propagating in low-$\boldsymbol{B}$ regions, quasi-parallel to $\boldsymbol{B}(t)$. We show that the underlying source of excitation is the pressure anisotropy of electrons and ions trapped in mirror modes with loss-cone-type distributions. We also observe that IC waves play an essential role in regulating the ion pressure anisotropy at nonlinear stages. We argue that whistler and IC waves are a concomitant feature at late stages of the mirror instability even at high β, and therefore, expected to be present in astrophysical environments like the ICM. We discuss the implications of our results for collisionless heating and dissipation of turbulence in the ICM.

Unified Astronomy Thesaurus concepts: Plasma astrophysics (1261); Intracluster medium (858); Galaxy clusters (584); Extragalactic magnetic fields (507); High energy astrophysics (739)

Supporting material: animations

1. Introduction

Several classes of astrophysical plasmas display fully developed turbulent states and a weak collisionality, in the sense that the particles' mean free path is several orders of magnitude larger than the typical radius at which they gyrate around the ambient magnetic field. These two characteristics alone can make the transport properties and global evolution of the astrophysical environment in question challenging and dependent on the local evolution at particle scales. Therefore, a detailed study of the behavior of these plasmas at the kinetic level becomes a necessity.

That is the case of the intracluster medium (ICM) of galaxy clusters. The ICM is a hot, magnetized (Bonafede et al. 2010), weakly collisional, and turbulent (Schuecker et al. 2004; Zhuravleva et al. 2014; Hitomi Collaboration et al. 2016) gas in the plasma state where the thermal pressure greatly exceeds the magnetic pressure ($\beta \equiv 8\pi P/B^2 \sim 10$–$100$, P is the isotropic thermal pressure and B the magnetic field strength). In these conditions, departures from thermodynamic equilibrium, such as pressure anisotropies, are easy to achieve. For example, slow compression of the magnetic field increases particle kinetic energy perpendicular to the magnetic field such that the magnetic moment (or the magnetic flux through the particle gyro-orbit) remains constant, leading to an excess of perpendicular pressure $P_\perp$ over parallel pressure $P_\parallel$. However, pressure anisotropy cannot grow unchecked. Pressure anisotropies can easily destabilize microinstabilities such as mirror, firehose, ion cyclotron (IC), and whistler (Schekochihin et al. 2005; Schekochihin & Cowley 2006). The backreaction of these instabilities on the particles can maintain pressure anisotropy near its marginally unstable value, and are thought to play an important role in several aspects of ICM transport and heating (Kunz et al. 2011; Berlok et al. 2021; Drake et al. 2021; Perrone & Latter 2022a, 2022b; Ley et al. 2023; Tran et al. 2023).

In a similar vein, the solar wind and some regions of the Earth's magnetosheath and magnetosphere host plasmas that are also collisionless and turbulent. Even when the plasma β is lower than in the ICM ($\beta_i \sim 1$–10, $\beta_e \sim 1$) we can encounter some similarities. In particular, the plasma is also pressure anisotropic, and the same abovementioned microinstabilities are found to be present, usually in their fully developed, nonlinear stage (Bale et al. 2009). Particularly important to this work is the presence of the mirror instability (Chandrasekhar et al. 1958; Rudakov & Sagdeev 1961; Hasegawa 1969; Southwood & Kivelson 1993; Kivelson & Southwood 1996; Pokhotelov et al. 2002, 2004) and its interplay with the whistler and (potentially) IC instabilities (Gary 1992; Gary & Wang 1996). An example of this has been observed in these space plasmas, and termed whistler lion roars.

Whistler lion roars are short bursts of right-handed polarized waves, with frequencies below the electron-cyclotron frequency ($\omega_{c,e}$) commonly observed in the Earth's magnetosheath and

magnetosphere (Smith et al. 1969; Tsurutani et al. 1982; Baumjohann et al. 1999; Breuillard et al. 2018; Giagkiozis et al. 2018; Kitamura et al. 2020; Zhang et al. 2021), therefore identified as whistler waves. They have also been observed in Saturn's magnetosheath (Píša et al. 2018) and the solar wind. They are observed in regions of locally low magnetic field strength (magnetic troughs, or magnetic holes) of magnetic fluctuations. These magnetic troughs are usually identified as structures produced by mirror instability modes, which are able to trap electrons with low parallel velocity within these regions, due to the aforementioned invariance of magnetic moment (Southwood & Kivelson 1993).

Several mechanisms have been proposed to explain the excitation of whistler lion roars. They usually invoke the pressure anisotropy $P_{\perp,e} > P_{\parallel,e}$ that electrons generate while trapped inside the magnetic troughs ($P_{\perp,e}$ and $P_{\parallel,e}$ are, respectively, the electron pressure perpendicular and parallel with respect to the local magnetic field $\boldsymbol{B}$). Other mechanisms have also been proposed involving counter-propagating electron beams inside these regions, and butterfly distributions in pitch-angle (Zhang et al. 2021; Jiang et al. 2022). As the waves propagate out from the magnetic troughs, they are thought to interact with electrons, regulating the number of trapped electrons inside magnetic troughs and also the global anisotropy of electrons in the magnetosheath. This way, there would be a causal connection between an ion-scale mirror instability with an electron-scale whistler instability at nonlinear stages, providing valuable insight into the interaction of mirror modes with electrons.

The question arises as to whether a similar interplay can be expected in the ICM. Such behavior would imply a more complex scenario in which several microinstabilities would be causally connected and coexisting with each other, and several channels of turbulent energy dissipation would open, leading to much richer dynamics.

Mirror instability and its consequences have been extensively studied using particle-in-cell (PIC) simulations of moderately and high-β plasmas, both hybrid (Kunz et al. 2014; Melville et al. 2016; Arzamasskiy et al. 2023) and fully kinetic (Riquelme et al. 2015; Sironi & Narayan 2015; Riquelme et al. 2016; Ley et al. 2023), up to nonlinear stages. Consistent with early theoretical works (Southwood & Kivelson 1993; Kivelson & Southwood 1996), it has been demonstrated that mirror modes are efficient in trapping ions inside regions of low magnetic field strength during their secular growth (Kunz et al. 2014). When mirror modes reach amplitudes of order $\delta B/B \sim 1$, they reach a saturated stage and the ions eventually undergo scattering, allowing them to escape. This trapping process is similar for electrons, and it has been shown to have important consequences in the electron viscosity and thermal conduction of the plasma (Riquelme et al. 2016; Roberg-Clark et al. 2016, 2018). Interestingly, Riquelme et al. (2016) reported the observation of whistler waves in the nonlinear, saturated stages of mirror modes in their simulations, along with IC waves, although they did not pinpoint the cause of the excitation.

In this work, we use PIC simulations to investigate the nonlinear stages of the mirror instability at moderate and high β, focusing on the abovementioned excitation of whistler and IC waves. We observe that, indeed, both right-handed and left-handed polarized, quasi-parallel-propagating waves are excited at the end of the mirror's secular growth and during its saturated stage, and provide evidence for their excitation mechanism associated with the pressure anisotropy electrons and ions within magnetic troughs of mirror modes. The right- and left-handed circular polarization of these waves leads to their identification as electron-cyclotron (i.e., whistlers) and IC waves. We also provide an additional discussion about their nature. We describe the interaction of these waves with electrons and ions, and their effect on the regulation of the pressure anisotropy at late stages.

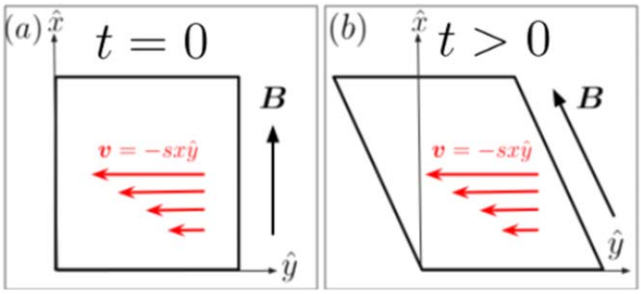

Figure 1. The evolution of the simulation domain. Panel (a): initially, the box is straight, the magnetic field is initialized pointing in the $\hat{x}$ direction and a shear velocity field $\boldsymbol{v} = -sx\hat{y}$ is imposed in the y-direction (red arrows). Panel (b): the velocity field shears the box continuously throughout the simulation, amplifying the magnetic field and changing its direction in the process due to magnetic flux conservation.

This paper is organized as follows. Section 2 describes our simulation setup and the runs we perform. Section 3 shows our simulation results starting from the excitation of the mirror instability, an early whistler burst, and then the late excitation of the electron and IC waves at nonlinear stages of the mirror instability. We also detail the mechanism by which these cyclotron waves are excited during the saturated stage of mirror modes, by tracking ions and electrons throughout the simulations. We also describe the subsequent interaction of these waves with the ions and electrons at late stages. In Section 4, we discuss the dependence of our results on the mass ratio used in our simulations and show that they are fairly insensitive to it. In Section 5, we present the results of simulations at different initial ion plasma betas, and show these cyclotron waves are also present at lower and higher betas as well. Finally, we discuss the implication of our work in the context of galaxy clusters and present our conclusions in Section 6.

2. Simulation Setup

We perform fully kinetic, 2.5D PIC simulations using TRISTAN-MP (Buneman 1993; Spitkovsky 2005), in which we continuously shear a collisionless, magnetized plasma composed of ions and electrons (Riquelme et al. 2012). The magnetic field is initially spatially uniform and starts pointing along the x-axis. A shear velocity field is imposed with $\boldsymbol{v} = -sx\hat{y}$ (red arrows in Figure 1), where x is the distance along the x-axis and s is a constant shear rate. We solve the PIC system of equations using shearing coordinates, as implemented in Riquelme et al. (2012). (The suitability of this approach to studying ion Larmor scale phenomena is also discussed in Riquelme et al. 2015.) The conservation of magnetic flux implies that the y-component of the magnetic field $\boldsymbol{B}$ evolves as $dB_y/dt = -sB_0$, whereas $dB_x/dt = 0$ and $dB_z/dt = 0$. The action of the shear then continuously amplifies the magnetic

Table 1
Simulations and Their Physical and Numerical Parameters

Runs	$\beta_i^{\rm init}$	m_i/m_e	$\omega_{c,i}^{\rm init}/s$	$\frac{k_B T}{m_i c^2}$	$N_{\rm ppc}$	$L/R_{L,i}^{\rm init}$
b20m8w800	**20**	**8**	**800**	**0.02**	**600**	**54**
b20m32w800	20	32	800	0.01	300	50
b20m64w800	20	64	800	0.01	200	40
b40m8w800	40	8	800	0.02	300	49
b2m8w800	2	8	800	0.02	300	68

Note. The physical parameters of the simulations are the initial ion plasma beta $\beta \equiv 8\pi P_i^{\rm init}/B^2$, where $P_i^{\rm init}$ is the initial ion pressure, the mass ratio between ions and electrons m_i/m_e, and the magnetization $\omega_{c,i}/s$. The numerical parameters are the number of particles per cell $N_{\rm ppc}$ and the domain size in terms of the initial ion Larmor radius $L/R_{L,i}^{\rm init}$. Our fiducial simulation is highlighted in bold.

field strength such that its magnitude evolves as $B(t) = B_0\sqrt{1 + s^2t^2}$.

In our simulations, ions and electrons are initialized with Maxwell–Jüttner distributions (the relativistic generalization of the Maxwell–Boltzmann distribution; Jüttner 1911) with equal initial temperatures $T_i^{\rm init} = T_e^{\rm init}$, and $k_B T_i^{\rm init}/m_i c^2$ between 0.01 and 0.02. The physical parameters of our simulations are the initial temperature of ions and electrons ($T_i^{\rm init} = T_e^{\rm init}$), the initial ion plasma beta, $\beta_i^{\rm init}$, the mass ratio between ions and electrons m_i/m_e, and the ratio between the initial IC frequency and the shear frequency, $\omega_{c,i}^{\rm init}/s$, that we call the *scale separation ratio*. The numerical parameters in our simulations are the number of macroparticles per cell, $N_{\rm ppc}$, the plasma skin depth in terms of grid point spacing, $c/\sqrt{\omega_{p,e}^2 + \omega_{p,i}^2}/\Delta x$, and the domain size in terms of the initial ion Larmor radius, $L/R_{L,i}^{\rm init}$, where $R_{L,i}^{\rm init} = v_{{\rm th},i}/\omega_{c,i}^{\rm init}$ and $v_{th,i}^2 = k_B T_i/m_i$. These physical and numerical parameters are listed in Table 1. We fix $c/\sqrt{\omega_{p,e}^2 + \omega_{p,i}^2}/\Delta x = 3.5$ in the simulations presented in Table 1.

In the majority of the paper, we discuss a representative, fiducial simulation with $m_i/m_e = 8$, $\beta_i^{\rm init} = 20$ (thus, $\beta^{\rm init} = \beta_i^{\rm init} + \beta_e^{\rm init} = 40$) and $\omega_{c,i}^{\rm init}/s = 800$ (simulation b20m8w200 in Table 1, highlighted in boldface). We vary the above parameters in a series of simulations, all listed in Table 1. Importantly, given the available computational capabilities, performing a simulation with a realistic mass ratio $m_i/m_e = 1836$ becomes prohibitively expensive. Therefore, a range of values of ion-to-electron mass ratio are presented in order to ensure that our results do not strongly depend on this parameter. The effects of varying these parameters are discussed in Sections 4 and 5.

In the absence of a scattering mechanism and/or collisions, the ion and electron magnetic moments $\mu_j \equiv p_{\perp,j}^2/(2m_j B)$ and longitudinal action $\mathcal{J}_j \equiv \oint p_{j,\parallel} d\ell$ are adiabatic invariants ($p_{\perp,j}$ and $p_{\parallel,j}$ are the components of the momentum of a particle of species j perpendicular and parallel to the local magnetic field, respectively, and $j = i$, e), and therefore, are conserved as the system evolves, provided that the variation of $\boldsymbol{B}$ is sufficiently slow compared to the particle cyclotron frequencies; in our case, $s \ll \omega_{c,j}$, where $\omega_{c,j} = eB/m_j c$ is the cyclotron frequency of particles of species j, c is the speed of light, and e is the magnitude of the electric charge.

The continuous amplification of the magnetic field $\boldsymbol{B}$ implies that the particles' adiabatic invariance drives a pressure anisotropy in the plasma such that $P_{\perp,j} > P_{\parallel,j}$. In the very early stages of the simulation, we expect the evolution of $P_{\perp,j}$ and $P_{\parallel,j}$ to be dictated by double-adiabatic scalings (Chew et al. 1956). Soon after this stage, however, the pressure anisotropy acts as a free energy source in the plasma and is able to excite several kinetic microinstabilities after surpassing their excitation thresholds, which are proportional to $\beta^{-\alpha}$, ($\alpha \sim 0.5$–1) (Hasegawa 1969; Gary & Lee 1994; Gary & Wang 1996). These microinstabilities break the adiabatic invariants and act upon the pressure anisotropy to regulate the anisotropy growth in the nonlinear stages.

In our simulations, and given our initial physical parameters (namely, $\beta_i^{\rm init} \equiv 8\pi P_i^{\rm init}/B^{2{\rm init}} = 20$), we expect the dominant instability to be the mirror instability. Mirror modes are purely growing (i.e., zero real frequency), with the fastest growing modes propagating highly obliquely with respect to the mean magnetic field. Their most unstable wavenumbers satisfy $k_\perp R_{L,i} \sim 1$, where $R_{L,i}$ is the ion Larmor radius. This instability presents Landau resonances with particles of very small parallel momentum, $p_\parallel \approx 0$, that become trapped in between mirror modes, and contribute to regulating the pressure anisotropy.

In addition to the mirror instability, we also observe wave activity that we associate with the IC (Gary 1992) and whistler (Gary & Wang 1996) instabilities at ion and electron scales, respectively, during the late stages of our simulations. IC modes are left-handed circularly polarized and have a real frequency below the IC frequency $\omega_{c,i}$, with modes of maximum growth rate propagating parallel to the mean magnetic field $\boldsymbol{B}$. Similarly, whistler modes are right-handed circularly polarized and have a real frequency below the electron-cyclotron frequency $\omega_{c,e}$, with modes of maximum growth rate also propagating parallel to $\boldsymbol{B}$. As we will see, this wave activity is associated with the ion and electron trapping processes that mirror modes generate.

3. Results

Figures 2 and 3 summarize the evolution of magnetic field fluctuations and particle pressure anisotropy over time.

Figure 2 shows the fluctuations in the magnetic field $\delta\boldsymbol{B} \equiv \boldsymbol{B} - \langle \boldsymbol{B} \rangle$ (where $\langle \cdot \rangle$ denotes a volume average over the entire simulation domain) in its three different components at two different times: $t \cdot s = 0.4$ (first row, panels (a)–(c)) and at $t \cdot s = 1.4$ (second row, panels (d)– (f)). The black arrows in panels (a)–(f) denote the direction of the mean magnetic field $\langle \boldsymbol{B} \rangle$ at those particular times. The components of $\delta\boldsymbol{B}$ are defined as parallel with respect to the main field $\langle \boldsymbol{B} \rangle$ ($\delta B_\parallel$, panels (b) and (e)), perpendicular to $\langle \boldsymbol{B} \rangle$ in the plane of the simulation ($\delta B_{\perp,xy}$, panels (a) and (d)) and perpendicular to $\langle \boldsymbol{B} \rangle$ in the direction out of the simulation plane (δB_z, panels (c) and (f)). Additionally, Figure 2(g) shows the evolution of the energy in each of the three components of $\delta\boldsymbol{B}$, normalized by $B(t)^2$; $\delta B_\parallel^2$ (blue line), $\delta B_{\perp,xy}^2$ (red line), and δB_z^2 (green line).

Figure 3(a) shows the evolution of the ion pressure anisotropy $\Delta P_i \equiv P_{\perp,i} - P_{\parallel,i}$ for run b20m8w800, and the gray-dashed line shows the approximate instability threshold for the mirror instability (Hasegawa 1969; Hellinger 2007). We can see that the ion anisotropy surpasses the mirror threshold very early in the simulation, and reaches its maximum value at $t \cdot s \approx 0.5$ (we will call this stage the anisotropy overshoot,

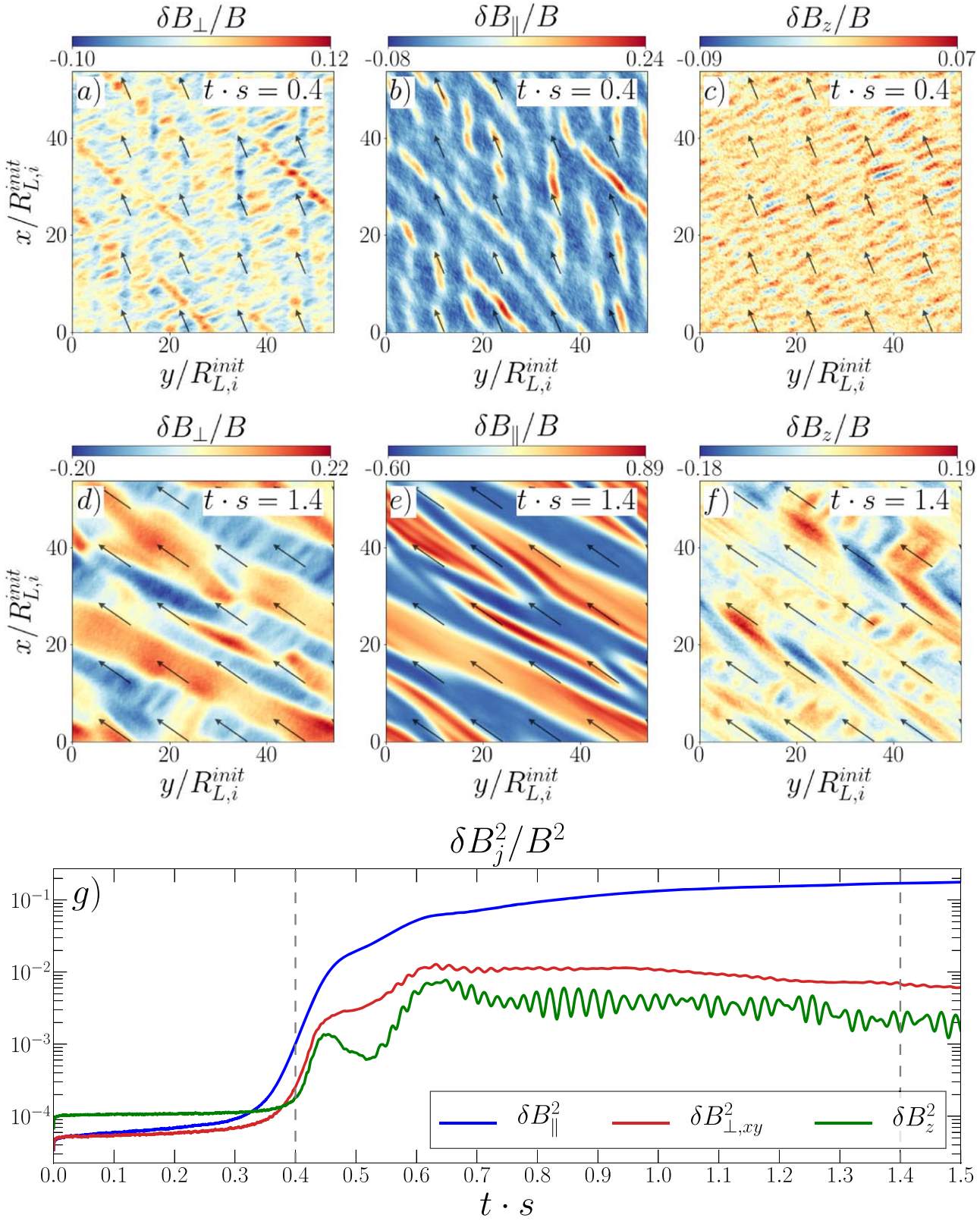

Figure 2. First row: the different component of magnetic fluctuations $\delta \boldsymbol{B} = \boldsymbol{B} - \langle \boldsymbol{B} \rangle$ for run b20m8w800 in the simulation domain at $t \cdot s = 0.4$: $\delta B_\perp$. Panel (a) is the component perpendicular to the main field $\langle \boldsymbol{B} \rangle$ in the x-y plane of the simulation, $\delta B_\parallel$. Panel (b) is the component parallel to $\langle \boldsymbol{B} \rangle$ and δB_z. Panel (c) is the component perpendicular to $\langle \boldsymbol{B} \rangle$ in the direction out of the plane of the simulation. Second row: panels (d)–(f) show the same as panels (a)–(c), but at $t \cdot s = 1.4$. Third row: the evolution of the energy in the three components of the magnetic field fluctuations $\delta \boldsymbol{B}$ normalized to $B(t)^2$, $\delta B_\parallel^2$ (blue line), $\delta B_{\perp,xy}^2$ (red line), and δB_z^2 (green line). The gray-dashed lines indicate the time at which the fluctuations in the first and second rows are shown. An animated version of this figure is available in the HTML version of this paper. The animation shows the evolution throughout the simulation of $\delta B_\perp$, $\delta B_\parallel$, and δB_z as well as $\delta E_\perp$, $\delta E_\parallel$, and δE_z, the electric field fluctuations (not shown in the static figure), and panel (g). The evolution runs from $t \cdot s = 0$–2.0.

(An animation of this figure is available.)

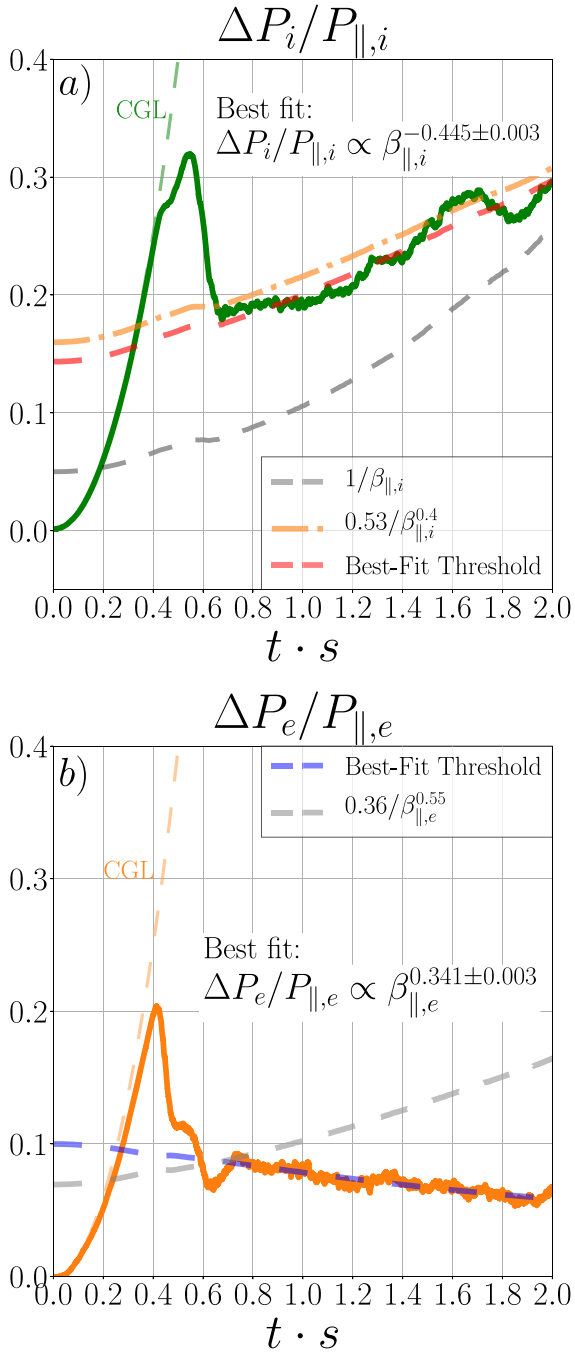

Figure 3. Panel (a): the evolution of the ion pressure anisotropy $\Delta P_i/P_{\|,i}$ for run b20m8w800 is shown as a solid green line. The green-dashed line shows the double-adiabatic evolution of $\Delta P_i/P_{\|,i}$ (Chew et al. 1956). The gray-dashed line shows the approximate threshold for the mirror instability: $1/\beta_{\|,i}$ (Hasegawa 1969). The orange-dashed–dotted line shows the threshold for the IC instability from Gary & Lee (1994) for $\gamma_{\rm IC}/\omega_{c,i} = 10^{-2}$ ($\gamma_{\rm IC}$ is the IC growth rate). The red-dashed line shows the best fit to $\Delta P_i/P_{\|,i} = A_i\beta_{\|,i}^{\alpha_i}$ from $t \cdot s = 0.7$–2.0, with $A_i = 0.544 \pm 0.003$ and $\alpha_i = 0.445 \pm 0.003$. Panel (b): the evolution of the electron pressure anisotropy $\Delta P_e/P_{\|,e}$ is shown as a solid orange line. The orange-dashed line shows the double-adiabatic evolution of $\Delta P_e/P_{\|,e}$. The blue-dashed line shows the best fit to $\Delta P_e/P_{\|,e} = A_e\beta_{\|,e}^{\alpha_e}$ from $t \cdot s = 0.7$–2.0, with $A_e = 0.036 \pm 0.0002$ and $\alpha_e = 0.341 \pm 0.003$. The gray-dashed line shows the linear threshold for the anisotropic whistler instability from (Gary & Wang 1996) for growth rate $\gamma_{\rm W}/\omega_{c,e} = 0.01$. ($\gamma_{\rm W}$ is the whistler growth rate).

hereafter). We will show that this is consistent with the beginning of the secular growth of mirror modes (Kunz et al. 2014; Riquelme et al. 2016). Figure 3(b) shows the same for the electron pressure anisotropy, which we will show relaxes by efficient scattering.

3.1. Evolution of Mirror Instability

Since mirror modes are highly oblique, their evolution is well represented by the time trace of $\delta B_\|^2$ shown in Figure 2(g). We identify both a linear, exponentially growth phase until $t \cdot s \approx 0.45$, and a subsequent nonlinear, slower-growing secular phase, consistent with the different evolutionary phases of the ion and electron pressure anisotropies described above. Besides the break in the evolution of the mirror mode at $t \cdot s \approx 0.45$, a second break in the secular growth occurs around $t \cdot s = 0.6$ followed by a shallower slope of growth. We will show that this break coincides with the excitation of both whistler and IC waves in $\delta B_{\perp,xy}^2$ and δB_z^2, implying that whistler and IC waves, albeit smaller in amplitude, modulate the evolution of mirror modes during nonlinear stages.

3.1.1. Linear, Exponentially Growing Mirror Phase

After an early Chew, Goldberger, Low (CGL; Chew 1956) phase of the pressure anisotropy ΔP_j ($j = i$, e, see Figure 3), Figure 2(g) shows the excitation of the mirror instability starting at $t \cdot s \approx 0.35$, mainly in the parallel component of the magnetic fluctuations, $\delta B_\|$ (blue line), consistent with theoretical expectations (Southwood & Kivelson 1993; Pokhotelov et al. 2004). Figure 2(g) also shows that $\delta B_\|$ grows first and it has the largest amplitude throughout the entire simulation, meaning that the mirror instability is indeed the dominant instability.

Figure 2(b) (i.e., $\delta B_\|^2$) shows the linear, exponentially growth phase of mirror modes at $t \cdot s = 0.4$, where small filamentary structures of high local magnetic field amplitude start to emerge and slowly grow, in between wider regions of low local magnetic field amplitude. The obliqueness of the modes is readily apparent, as well as the fact that the mirror-generated magnetic fluctuations lie mainly in the $(\boldsymbol{k}, \boldsymbol{B})$ plane (they can be seen in $\delta B_{\perp,xy}^2$ too, but not in δB_z^2, as expected from linear theory; Pokhotelov et al. 2004). The oblique nature of mirror modes can also be seen in Figure 4(a), where we show the power spectrum in space of $\delta B_\|$ at $t \cdot s = 0.4$. The solid and dashed lines represent the directions parallel and perpendicular to the mean magnetic field $\langle \boldsymbol{B} \rangle$, respectively. Therefore, we can see that at $t \cdot s = 0.4$, the power is mostly concentrated between wavevectors $0.44 \lesssim kR_{L,i}^{\rm init} \lesssim 1.35$ and angles of $52° \lesssim \theta_k \lesssim 77°$, where $\theta_k \equiv \cos^{-1}(\boldsymbol{k} \cdot \langle \boldsymbol{B} \rangle / kB)$ is the angle between the mirror modes' wavevector and the mean magnetic field $\langle \boldsymbol{B} \rangle$.

It should be emphasized that the IC wave activity only starts at $t \cdot s = 0.6$, and not before. There is no sign of an early excitation of the IC instability competing with the mirror instability for the available free energy in $\Delta P_i/P_{\|,i}$. Instead, at earlier stages, only the mirror instability is excited, consistent with our initial conditions of high beta ($\beta_i^{\rm init} = 20$), where the mirror instability is expected to dominate (e.g., Riquelme et al. 2015).

The absence of IC waves early in the simulation ($0 < t \cdot s < 0.6$) can clearly be seen in Figure 5(a), where we show the power spectrum in time and space of $\delta B_z(\omega, k_\|) + i\delta B_{\perp,xy}(\omega, k_\|)$ at early stages: $0.3 < t \cdot s < 0.5$. This particular combination of the two perpendicular components of $\delta \boldsymbol{B}$ allows us to disentangle the parallel-propagating waves (with respect to the main magnetic field $\langle \boldsymbol{B} \rangle$, e.g., IC and

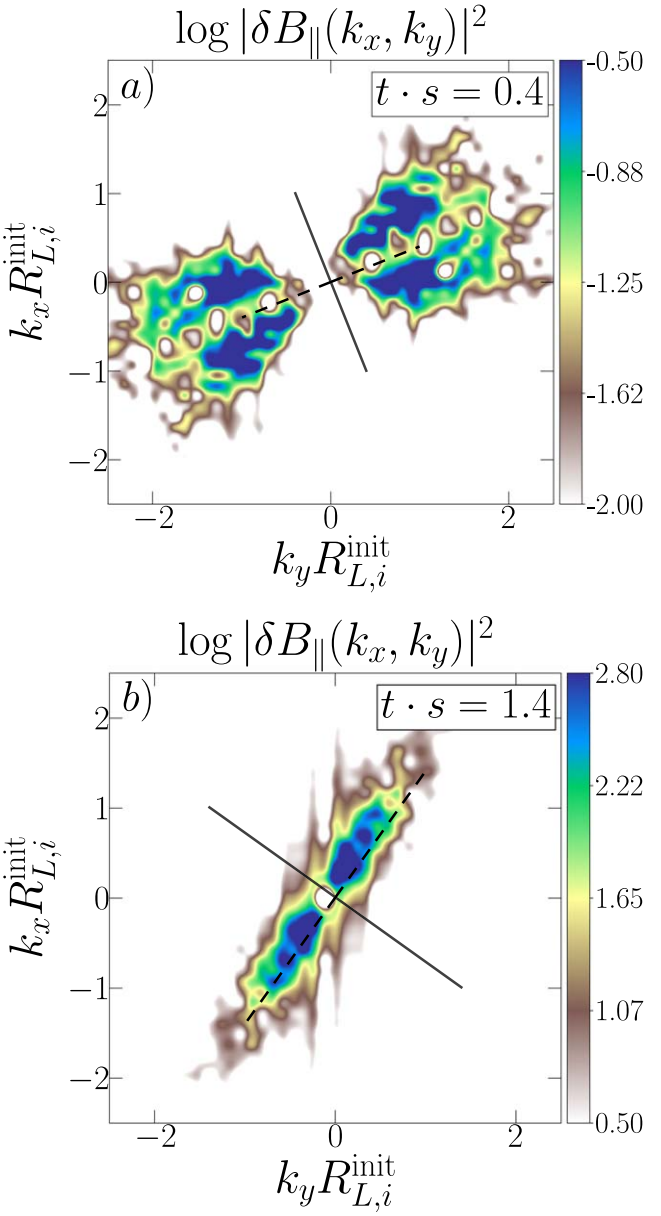

Figure 4. Panel (a): power spectrum in space of $\delta B_{\parallel}(k_x, k_y)$ at $t\cdot s = 0.4$. The wavenumbers k_x, k_y are normalized by the initial Larmor radius of the ions, $R_{L,i}^{\rm init}$. The solid and dashed black lines represent the direction parallel and perpendicular to the main magnetic field at that time, respectively. Panel (b): power spectrum in space of $\delta B_{\parallel}(k_x, k_y)$ at $t\cdot s = 1.4$. Note that the scale of color bars in panels (a) and (b) are different.

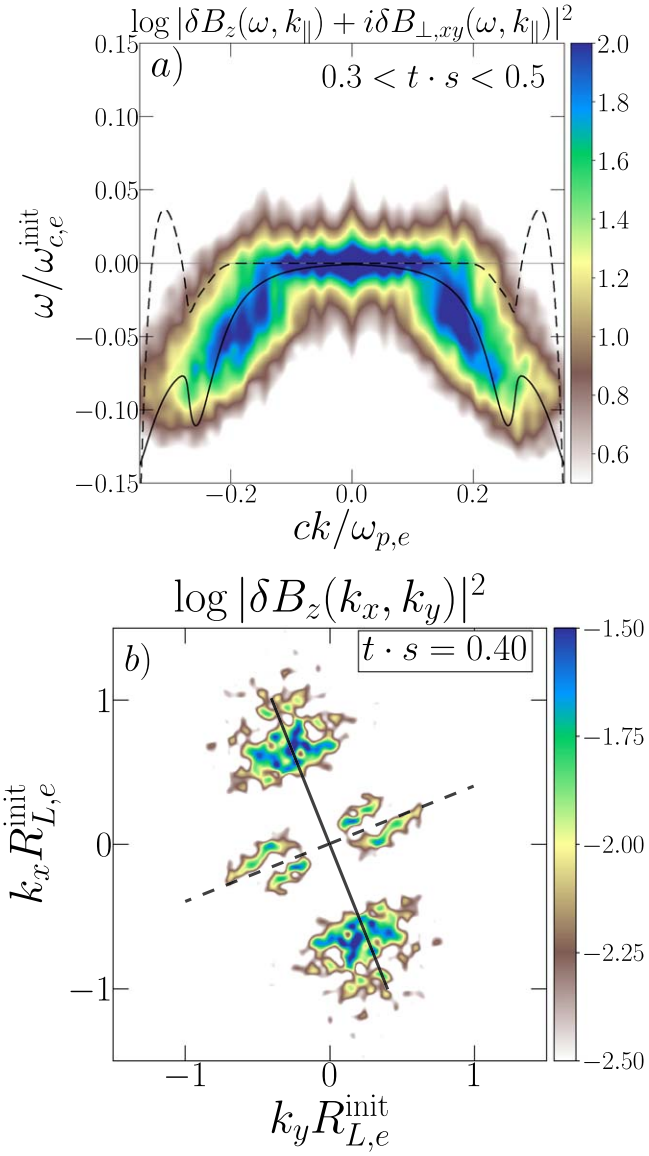

Figure 5. Panel (a): the power spectrum of $\delta B_z(\omega, k_{\parallel}) + i\delta B_{\parallel,xy}(\omega, k_{\parallel})$ in the entire simulation domain and between $0.3 < t\cdot s < 0.5$. The frequency is normalized by the initial electron-cyclotron frequency $\omega_{c,e}$, and the wavevector is normalized by the plasma frequency $\omega_{p,e}$ over the speed of light c. The solid black line shows the linear dispersion relation $\omega_r(k)$ for the whistler instability according to our linear dispersion solver, whereas the black-dashed line shows its growth rate γ. Panel (b): the power spectrum in space of $\delta B_z(k_x, k_y)$ at $t\cdot s = 0.4$. The wavenumbers k_x, k_y are normalized to the initial Larmor radius of the electrons, $R_{L,e}^{\rm init}$. The solid and dashed black lines represent the direction parallel and perpendicular to the main magnetic field at that time.

whistlers), and also their left-handed and right-handed circular polarizations (Ley et al. 2019; Tran et al. 2023). In this case, the left-handed circularly polarized wave activity is shown for $\omega > 0$, whereas the right-handed circularly polarized wave activity is shown for $\omega < 0$. We can readily see that, apart from the $\omega \approx 0$ power consistent with mirror modes appearing in $\delta B_{\perp,xy}$, there is no left-handed polarized wave activity throughout $0.3 < t\cdot s < 0.5$, only right-handed polarized waves, which corresponds to an early excitation of the whistler instability, as we will see in Section 3.2.

3.1.2. Nonlinear, Secular Mirror Phase

At $t\cdot s \approx 0.45$, we can clearly see the beginning of the secular growth of the mirror instability, where the modes reach nonlinear amplitudes, and keep growing but at a slower rate. This evolution is consistent with previous works (Kunz et al. 2014; Riquelme et al. 2016).

Interestingly, the mirror secular growth is interrupted at $t\cdot s \approx 0.6$, and the slope of $\delta B_{\parallel}^2$ breaks. This is also approximately where the ion pressure anisotropy experiences its fastest decline (Figure 3). Mirror modes continue to grow, but at a much slower rate. This is consistent with the saturation of energy in the subdominant components $\delta B_{\perp,xy}^2$ and δB_z^2 (solid red and green lines in Figure 2(g), respectively), which also presents a distinct pattern of oscillations. This activity is clear evidence of a new burst of waves with components mainly in the direction perpendicular to $\delta \boldsymbol{B}$, and we will see that they are

consistent with both electron-cyclotron waves (whistlers) and IC waves excited by electron and ion populations, respectively, that become trapped within mirror modes (see Section 3.3).

Figure 2(e) shows a late, nonlinear stage of the mirror instability, at $t \cdot s = 1.4$. At this time, the regions of high magnetic field of mirror modes (e.g., red filamentary structures seen in Figure 2(b)) have grown significantly and merged with neighboring structures to form wider and sharper regions of high local amplitudes ($\delta B_{\parallel}/B \sim 0.9$), whose sizes are comparable to regions of low magnetic field. At this stage, most of the power is concentrated in wavevectors $0.2 \lesssim kR_{L,i}^{\rm init} \lesssim 1.1$, and angles $57^{\circ} \lesssim \theta_k \lesssim 85^{\circ}$ (see Figure 4(b)).

After reaching its overshoot, the ion anisotropy starts to decrease toward marginal stability. However, this decrease stops around $t \cdot s \approx 0.65$ at $\Delta P_i/P_{\parallel,i} \approx 0.18$, well above the approximate mirror threshold (gray-dashed line, Hasegawa 1969; Hellinger 2007). The anisotropy then reaches a marginal stability level that is above the mirror threshold, similar to some previous works using both hybrid and fully kinetic simulations (Sironi & Narayan 2015; Melville et al. 2016; Ley et al. 2023).

In order to better characterize the evolution of $\Delta P_i/P_{\parallel,i}$, we fit a relation $\Delta P_i/P_{\parallel,i} = A_i \beta_{\parallel,i}^{\alpha_i}$ from $0.7 \leqslant t \cdot s \leqslant 2$. (In our simulations, the shear motion continuously amplifies $\boldsymbol{B}$; therefore, $\beta_{\parallel,i}$ also evolves.) As shown in Figure 3(a), our best-fit parameters are $A_i = 0.544 \pm 0.003$ and $\alpha_i = -0.445 \pm 0.003$. The obtained exponent is consistent with the marginal stability threshold given by the IC instability for lower β_i (Gary & Lee 1994). Indeed, the threshold for the IC instability, $\Delta P_i = 0.53\beta_{\parallel,i}^{-0.4}$, is plotted as the orange-dashed–dotted line in Figure 3(a) for $\gamma_{\rm IC}/\omega_{c,i} = 10^{-2}$ (Gary & Lee 1994), and we can clearly see the similarity with our best-fit threshold, even at this higher value of initial $\beta_{\parallel,i}^{\rm init}$. This observation was also reported in Sironi & Narayan (2015), and we will see that, indeed, we do observe IC waves as part of the saturated phase of the mirror instability that starts at $t \cdot s = 0.6$. The presence of ion and electron-cyclotron waves coexisting with mirror modes at late, nonlinear stages of the mirror instability has been reported in previous works (Sironi & Narayan 2015; Riquelme et al. 2016; Ahmadi et al. 2018). In Section 3.3, we argue that a natural explanation of the source of these cyclotron waves is the pressure anisotropy of ions trapped within nonlinear mirror modes.

3.2. First Whistler Burst: t · s ≈ 0.4

Figure 3(b) shows the evolution of the electron pressure anisotropy $\Delta P_e \equiv P_{\perp,e} - P_{\parallel,e}$ for run b20m8w800. Initially, the electrons develop their own pressure anisotropy alongside ions and for the same reasons. The anisotropy follows double-adiabatic (CGL) scaling (orange- dashed line) until $t \cdot s \approx 0.4$, when it has already reached a value significantly larger than the theoretical threshold for the growth of whistler modes, marked by gray-dashed lines (Gary & Wang 1996). Around this time, the whistler instability starts to grow, as seen by the time trace of δB_z^2 in Figure 2(g), which is a rough proxy for whistler waves, and also because there are no left-handed IC waves as shown in Figure 5(a). At $t \cdot s \approx 0.45$ the whistler modes saturate and enter a regime of quasi-steady amplitude, which lasts until $t \cdot s \approx 0.53$. During this $t \cdot s \approx 0.4$–0.53 period, ΔP_e is rapidly drawn down by frequent scattering, reaching a more slowly decreasing regime between $t \cdot s \approx 0.53$ and 0.6. The drawdown of electron anisotropy happens at a time when the ion anisotropy is still growing. This lasts until mirror modes are sufficiently high amplitude to start trapping the electrons ($t \cdot s = 0.6$).

The presence of whistler modes at $t \cdot s = 0.4$ can be seen mainly in the perpendicular components of $\delta \boldsymbol{B}$, namely, $\delta B_{\perp,xy}$ and δB_z, Figures 2(a) and (c), respectively. They propagate quasi-parallel to the main magnetic field $\boldsymbol{B}$ in a fairly homogeneous way inside the simulation domain. This quasi-parallel propagation can also be seen in Figure 5(b), where we show the power spectrum in space of $\delta B_z(k_x, k_y)$ at $t \cdot s = 0.4$ for run b20m8w800, and the solid and dashed black lines indicate the directions parallel and perpendicular to the main magnetic field $\langle \boldsymbol{B} \rangle$ at $t \cdot s = 0.4$. The power of $\delta B_z(k_x, k_y)$ is concentrated at parallel propagation and wavevectors $0.6 < kR_{L,e}^{\rm init} < 1$. This whistler burst is the first instability that is observed in our simulations, and before $t \cdot s = 0.4$ the plasma response is still consistent and well described by the double-adiabatic, CGL scalings, as shown in Figure 3(b).

We show the whistler wave frequencies in the power spectrum of $\delta B_z(\omega,\ k_{\parallel}) + i\delta B_{\perp,xy}(\omega,\ k_{\parallel})$ in the interval of $0.3 < t \cdot s < 0.5$ in Figure 5(a). We can see that the power is localized in the region $\omega < 0$, i.e., right-handed circularly polarized waves, consistent with the whistler polarization, and within frequencies of $0.02 < \omega/\omega_{c,e} < 0.05$. As mentioned above, no IC activity is present during this time period.

We also calculated the theoretical dispersion relation of the anisotropic whistler instability using a linear dispersion solver assuming an initial bi-Maxwellian distribution of electrons (Tran et al. 2023), using the initial parameters and values of $T_{\perp,e}$, $T_{\parallel,e}$ directly from the simulations. The dispersion relation $\omega(k)$ is shown as a solid black line in Figure 5(a), whereas the instability growth rate is shown in black-dashed lines. We can see that the power in right-handed circularly polarized waves is consistent with the whistler dispersion relation.

This way, the early evolution of the electrons is determined by an early burst of whistler modes associated with the initial electron pressure anisotropy growth. We will see that, once electrons start to become trapped in between mirror modes at $t \cdot s \approx 0.6$, another burst of whistler activity happens, this time associated with the trapping process within mirror modes during their secular and saturated phases.

3.3. Whistler and IC Excitations: t · s ≈ 0.6

At the end of its secular growth, when mirror modes have reached sufficiently high amplitudes, we simultaneously observe right-handed and left-handed circularly polarized wave activity, which we identify as whistler and IC waves, respectively. We will see below (Section 3.3) that these whistler and IC waves propagate mainly in regions of locally low magnetic fields (magnetic troughs). The source of this wave activity is identified to be the pressure anisotropic population of ions and electrons mainly due to trapped particles inside the magnetic troughs. The whistlers and IC waves then pitch-angle scatter both the trapped and untrapped particles, contributing to the regulation of the global anisotropy.

Figure 6 shows different spectral properties of the late burst of waves excited from $t \cdot s \approx 0.6$ onward. Figure 6(a) shows the power spectrum in time of $\delta B_z(\omega) + i\delta B_{\perp,xy}(\omega)$ between $0.5 < t \cdot s < 1.1$, so we can see both left-handed (solid blue line) and right-handed (solid orange line) circular polarizations. The power spectrum peaks at low frequencies, consistent with the nature of the dominant mirror modes (mainly appearing in

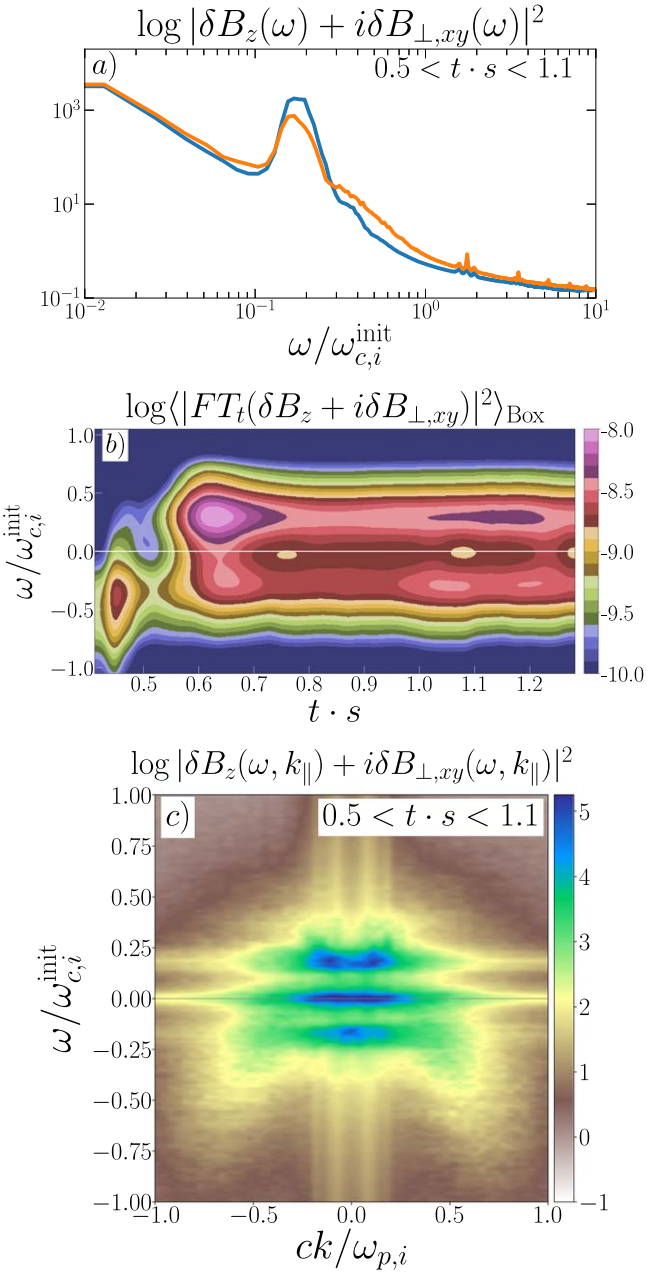

Figure 6. Panel (a): the power spectrum of $\delta B_z(\omega)+i\delta B_{\perp,xy}(\omega)$ as a function of frequency. The frequencies are normalized by the initial IC frequency. The power spectrum of left-handed circularly polarized waves ($\omega>0$) is shown as a solid blue line, whereas the power spectrum corresponding to right-handed circularly polarized waves ($\omega<0$) is shown as an orange line folded into positive frequencies. Panel (b): spectrogram of $\delta B_z(\omega)+i\delta B_{\perp,xy}(\omega)$ in frequency and time, at $0.4<t\cdot s<1.3$. The frequency is normalized by the initial IC frequency. Positive and negative frequencies correspond to left-handed and right-handed circularly polarized waves, respectively. Panel (c): the power spectrum of $\delta B_z(\omega,\ k_\parallel)+i\delta B_\perp(\omega,\ k_\parallel)$ at $0.5<t\cdot s<1.1$. Frequencies are normalized by the initial ion gyrofequency, and wavenumbers are normalized by the initial ion skin depth. Here also, positive and negative frequencies show left-handed and right-handed polarized waves, respectively.

$\delta B_{\perp,xy}$). Additionally, we can clearly see a secondary peak at around $\omega\sim0.2\omega_{c,i}$, with a spread that goes from $\omega\sim0.1\omega_{c,i}$ to $\omega\sim0.3\omega_{c,i}$, in both left- and right-handed circular polarizations. This constitutes the characteristic feature informing the late burst of wave activity. This peak resembles observations of whistler lion roars in the Earth's magnetosheath (see, e.g., Figures 1 and 2 of Giagkiozis et al. 2018; and Figure 3 of Zhang et al. 2021 for right-handed polarized waves.).

Figure 6(b) shows a spectrogram of $\delta B_z(\omega)+i\delta B_{\perp,xy}(\omega)$ in frequency and time, in the range of $0.4<t\cdot s<1.3$, with positive frequencies representing left-handed circularly polarized waves, and negative frequencies denoting right-handed circularly polarized waves. Here we can also see the early burst of whistler waves starting at $t\cdot s\approx0.4$ and peaking at $t\cdot s\approx0.45$ (see Section 3.2), followed by the burst of both left-handed and right-handed circularly polarized waves at $t\cdot s\approx0.53$ and peaking at $t\cdot s\approx0.65$. This coincides with the rise in amplitude of δB_z^2 and $\delta B_{\perp,xy}$ (see Figure 2(g)), and the waves are continuously maintained throughout the simulation at around the same frequencies.

Finally, Figure 6(c) shows the power spectrum of $\delta B_z(\omega,\ k_\parallel)+i\delta B_{\perp,xy}(\omega,\ k_\parallel)$ in time and space, at $0.5<t\cdot s<1.1$. Frequencies and wavenumbers are normalized by $\omega_{c,i}$ and $\omega_{p,i}/c$, respectively. Here we can also see the power at low frequencies consistent with the dominance of mirror modes appearing in $\delta B_{\perp,xy}$. The burst of left- and right-handed circularly polarized waves can be seen concentrated around frequencies $\omega\approx0.2\omega_{c,i}$ and $\omega\approx-0.15\omega_{c,i}$, respectively. Their range in wavenumbers is $0.2\lesssim ck_\parallel/\omega_{p,i}\lesssim0.5$. Overall, the power spectra of both left- and right-handed polarized waves are very similar to those of IC and electron cyclotron whistlers, and we will identify these waves as such from now on. In the next section, we will confirm that the population of particles that excites these waves have anisotropic distributions that are IC and whistler unstable.

The morphology of IC and whistler waves can also be seen in Figures 2(d) and (f). The short wavelength, wavepacket-like structures are identified with whistler modes, which propagate mainly through regions of low magnetic field strength of mirror modes, as can be seen from $\delta B_{\perp,xy}$ (blue-shaded regions in Figure 2(d)). The IC modes, on the other hand, are identified as the longer wavelength, extended modes that can be seen in δB_z (Figure 2(f)). The IC modes seem to propagate through the entire simulation box, given their ion-scale wavelength, whereas whistler modes clearly propagate within the mirrors' magnetic troughs. This also resembles magnetosheath's observations of whistler waves within magnetic troughs (e.g., Kitamura et al. 2020).

The peak frequencies observed in Figure 6 for both IC and whistler waves can be understood in terms of their dispersion relations. At high β and $kR_{L,e}\sim1$, and for quasi-parallel propagation, the dispersion relation for whistler waves can be written as (Stix 1992; Drake et al. 2021)

$$\omega_W=\omega_{c,e}k_W^2d_e^2=\omega_{c,i}k_W^2d_i^2, \tag{1}$$

where $d_e=c/\omega_{p,e}$ and $d_i=c/\omega_{p,i}$ are the electron and ion skin depths, respectively. Knowing that $d_i^2=R_{L,i}^2/\beta_i$, we can also write

$$\omega_W=\omega_{c,i}k_W^2R_{L,i}^2/\beta_i. \tag{2}$$

Similarly, at high β and $kR_{L,i}\sim1$, and for quasi-parallel propagation, the IC wave dispersion relation is approximately (Stix 1992)

$$\omega_{\rm IC}=\omega_{c,i}k_{\rm IC}d_i, \tag{3}$$

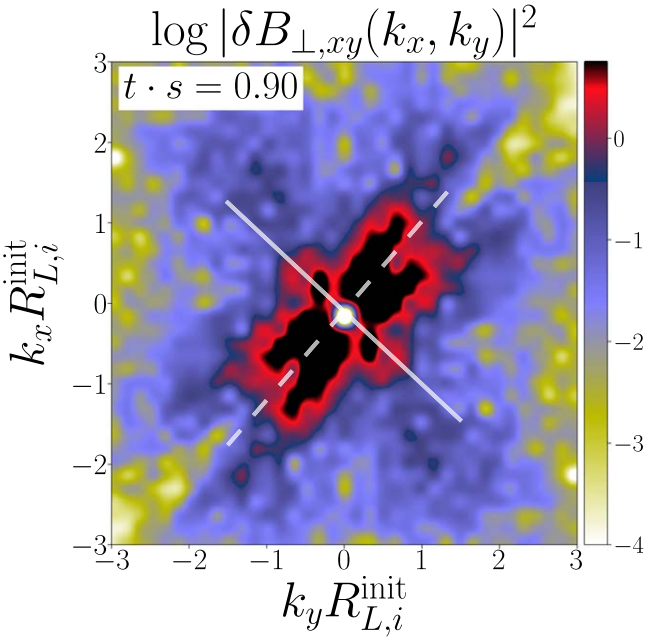

Figure 7. The power spectrum in space of $\delta B_{\perp,xy}(k_x, k_y)$ at $t\cdot s = 0.9$. The wavenumbers k_x, k_y are normalized by the initial ion Larmor radius $R_{L,i}^{\rm init}$. The solid and dashed white lines represent, respectively, the directions parallel and perpendicular to the main magnetic field at that time.

and we can also write

$$\omega_{\rm IC} = \omega_{c,i} k_{\rm IC} R_{L,i}/\sqrt{\beta_i}. \quad (4)$$

We can estimate k_W, $k_{\rm IC}$ by looking at the power spectrum of any of the perpendicular components of the magnetic field fluctuations. Figure 7 shows the power spectrum of $\delta B_{\perp,xy}(k_x, k_y)$ at $t\cdot s = 0.9$, where the solid and dashed white lines denote the direction parallel and perpendicular to the mean magnetic field $\boldsymbol{B}$ at that time, respectively. Apart from the power in the perpendicular direction corresponding to the mirror modes, in the power parallel to $\boldsymbol{B}$ (i.e., along the solid white line in Figure 7) we can distinguish large wavenumbers centered at $(k_y R_{L,i}^{\rm init}, k_x R_{L,i}^{\rm init}) \approx (0.75, -1.5)$ (and also at $(-1.5, 0.75)$), corresponding to whistlers, and also smaller wavenumbers centered at $(k_x R_{L,i}^{\rm init}, k_y R_{L,i}^{\rm init}) \approx (0.5, 0.7)$, corresponding to IC waves.

The large wavenumber extent in k_x, k_y observed in Figure 7 gives us an approximate range of wavenumbers of $1.5 \lesssim k_W R_{L,i}^{\rm init} \lesssim 3.2$ for whistlers, implying frequencies of $0.1 \lesssim \omega_W/\omega_{c,i}^{\rm init} \lesssim 0.5$ (as $\beta_i^{\rm init} = 20$), consistent with the frequencies observed in the negative half of Figure 6(c), corresponding to right-handed polarized waves. Similarly, the small wavenumber extent in k_x, k_y gives us a range of wavenumbers of $0.4 \lesssim k_W R_{L,i}^{\rm init} \lesssim 1.1$, implying frequencies of $0.1 \lesssim \omega_{IC}/\omega_{c,i}^{\rm init} \lesssim 0.25$, also consistent with the frequencies in the positive half of Figure 6(c), corresponding to left-handed polarized waves.

3.4. 2D Particle Distributions

The specific time at which ion and electron-cyclotron wave activity saturate, which coincides with the end of mirror instability's secular growth ($t\cdot s \approx 0.6$), and the propagation of whistler waves within regions of low magnetic field strength provide a hint toward uncovering the mechanism by which the whistler and IC waves are excited.

As a first step, we explore the evolution of the pressure anisotropy of ions and electrons at the time at which the IC and whistler waves are excited. At this time, mirror modes have achieved high amplitudes, and created sharp regions of high and low magnetic field strength, making the plasma spatially inhomogeneous. This implies that, in general, the plasma β of ions and electrons would not be the same at different locations in the simulation domain, making the anisotropy thresholds for the growth of the modes different in different regions. For this reason, a more appropriate method would be to measure the 2D distribution of pressure anisotropy, $\beta_\parallel$ and $\delta B_\parallel/B$, in the simulation domain.

Figure 8 shows the distribution of ion and electron pressure anisotropy as a function of ion $\beta_{\parallel,i}$ (panels (a)–(c)) and electron $\beta_{\parallel,e}$ (panels (g)–(i)), respectively, and the distribution of $\delta B_\parallel/B$ versus $\beta_{\parallel,i}$ (panels (d)–(f)) and electron $\beta_{\parallel,e}$ (panels (j)–(l)), respectively. These distributions are shown at three different times: the beginning of the simulation ($t\cdot s \approx 0$, left column); the end of the mirror's secular growth and the beginning of ion and electron-cyclotron wave activity ($t\cdot s = 0.6$, middle column), and a late stage well into the saturated regime of mirror instability ($t\cdot s = 1.4$, right column). In the top row of Figure 8 (i.e., panels (a)–(c)), the gray-dashed line corresponds to the approximate mirror instability threshold $1/\beta_{\parallel,i}$ (Hasegawa 1969), the orange-dashed–dotted line corresponds to the theoretical IC threshold $0.53/\beta_{\parallel,i}^{0.4}$ from Gary & Lee (1994) for $\gamma_{IC}/\omega_{c,i} = 10^{-2}$, and the solid black line represents the best-fit to the global ion anisotropy derived in Section 3.1 (see Figure 3(a)). In the third row of Figure 8 (panels (g)–(i)), the black-dashed–dotted line shows the whistler instability threshold of $0.36/\beta_{\parallel,e}^{0.55}$ from Gary & Wang (1996), for $\gamma_W/\omega_{c,e} = 10^{-2}$.

Starting with the ions, we can see that, from a stable, isotropic distribution at the very beginning of the simulation (Figure 8(a)), the ions become anisotropic enough to surpass both the mirror and the theoretical IC threshold from Gary & Lee (1994), as well as our best-fit instability threshold, as shown in Figure 8(b). At this point ($t\cdot s = 0.6$), we start to observe the excitation of IC waves that seem to interact with the ions and start driving them toward a marginally stable state. This can be seen in Figure 8(c), where the distribution becomes bimodal, with one population of ions under both the IC threshold and our best-fit threshold (centered at $\beta_{\parallel,i} \sim 5$ and $P_{\perp,i}/P_{\parallel,i} \sim 1.2$), meaning that they are driven toward marginal stability with respect to the IC threshold. Interestingly, there exists another ion population that is still unstable (centered at $\beta_{\parallel,i} \sim 18$ and $P_{\perp,i}/P_{\parallel,i} \sim 1.4$); therefore, IC waves could then continue being excited even at this late stage. This could explain the sustained amplitude observed in δB_z^2 and $\delta B_{\perp,xy}^2$ in Figure 2(g). Therefore, we can see that the unstable population has a higher $\beta_{\parallel,i}$, and the marginally stable population moves to lower $\beta_{\parallel,i}$.

For a similar value of $P_{\parallel,i}$, the difference in the values of $\beta_{\parallel,i}$ between the unstable and marginally stable populations should imply a difference in the local magnetic field strength (recall $\beta_{\parallel,i} = 8\pi P_{\parallel,i}/B^2$). This gives us a hint as to the location of the unstable and marginally stable populations in the domain, as mirror modes generate distinct regions of low and high magnetic field strength.

As can be seen in Figures 8(d)–(f), the ions also separate into two populations now in $\delta B_\parallel/B$. Starting from zero magnetic field fluctuations at the beginning ($t\cdot s \approx 0$, Figure 8(d)), we see how $\delta B_\parallel/B$ starts to grow at $t\cdot s = 0.6$ (Figure 8(e)), until we

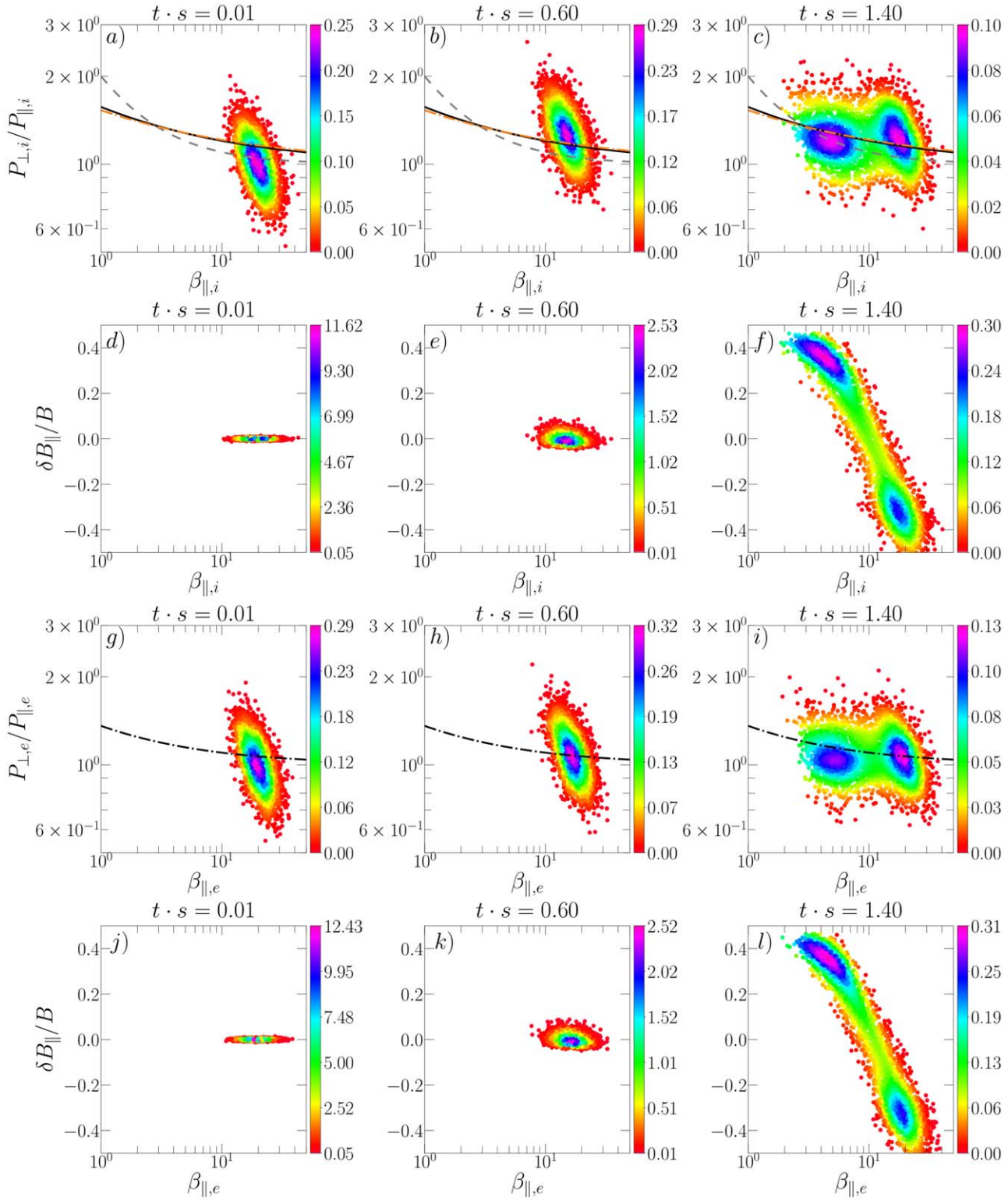

Figure 8. Top row: the distribution of ion $P_{\perp,i}/P_{\parallel,i}$ vs. $\beta_{\parallel,i}$ in the simulation domain at different times: $t \cdot s = 0.01$ (left column), $t \cdot s = 0.6$ (middle column), and $t \cdot s = 1.4$ (right column). The gray-dashed line represents the approximate mirror instability threshold $1/\beta_{\parallel,i}$ (Hasegawa 1969), and the orange-dashed–dotted line represents the IC instability threshold from Gary & Lee (1994) for $\gamma_{\rm IC}/\omega_{c,i} = 10^{-2}$ ($\gamma_{\rm IC}$ is the IC instability growth rate), and the solid black line represents our best-fit threshold from Section 3.1 (see Figure 3(a)). Second row: the distribution of $\delta B_\parallel/B$ vs. ion $\beta_{\parallel,i}$ for the same three times as in the top row. Third row: the distribution of electron $P_{\perp,e}/P_{\parallel,e}$ vs. $\beta_{\parallel,e}$ in the simulation domain at the same three times as in the top row. The black-dashed–dotted line represents the whistler instability threshold from Gary & Wang (1996). Fourth row: the distribution of $\delta B_\parallel/B$ vs. electron $\beta_{\parallel,e}$ for the same three times as in the top row. An animated version of this plot is available in the HTML version of this paper. The animation shows the evolution throughout the simulation of $P_{\perp,i}/P_{\parallel,i}$ vs. $\beta_{\parallel,i}$ and $\delta B_\parallel/B$ vs. ion $\beta_{\parallel,i}$ only for ions (i.e., the top two rows of the static figure only). The evolution runs from $t \cdot s = 0 - 1.5$.

(An animation of this figure is available.)

clearly see the bimodal distribution at $t \cdot s = 1.4$, separating the two ion populations: the high-$\beta_{\parallel,i}$ population located in regions of $\delta B_\parallel/B < 0$ (i.e., low-$\boldsymbol{B}$ strength), and the low-$\beta_{\parallel,i}$ population located in regions of $\delta B_\parallel/B > 0$ (i.e., high-$\boldsymbol{B}$ strength).

We can therefore conclude that, after mirror modes develop and the IC waves are excited ($t \cdot s \gtrsim 0.6$), the ions separate into two populations: one of low $\beta_{\parallel,i}$, located mainly in high-$\boldsymbol{B}$ strength regions, and marginally stable to IC waves, and the second population with high-$\beta_{\parallel,i}$, low-$\boldsymbol{B}$ strength regions, and still unstable to IC waves. This suggests that the IC waves are excited by the unstable ion populations in regions of low magnetic field strength, and then interact with the ions in such a way that the ions move to regions of high-$\boldsymbol{B}$ strength and low $\beta_{\parallel,i}$. In Sections 3.5 and 3.6 we will see that the population of ions that contribute most to the anisotropy that destabilizes the IC waves are the ones that become trapped within mirror troughs.

In the case of the electrons, we can see a similar evolution. From a stable, isotropic distribution at $t \cdot s \approx 0$ (Figure 8(d)), we can see how part of it now becomes whistler unstable at $t \cdot s = 0.6$ (Figure 8(e)), after which the excited whistler waves interact with the electrons driving again part of the distribution gradually toward marginal stability, also generating a bimodal distribution similar to that of the ions. At $t \cdot s = 1.4$ (Figure 8(f)), we can see that the electron population with low $\beta_{\parallel,e}$ (centered at $\beta_{\parallel,e} \sim 5$ and $P_{\perp,e}/P_{\parallel,e} \sim 1$) is marginally stable with respect to the whistler threshold, whereas the electron population with high $\beta_{\parallel,e}$ (centered at $\beta_{\parallel,e} \sim 18$ and $P_{\perp,e}/P_{\parallel,e} \sim 1.2$) is still unstable with respect to the whistler threshold. This also implies that whistler waves can still be excited at late stages in the simulation.

Analogously, the electrons also separate into two populations with respect to $\delta B_\parallel/B$. Similarly to ions, we also see that the population with low $\beta_{\parallel,e}$ is located in regions of $\delta B_\parallel/B < 0$ (low-$\boldsymbol{B}$ strength), whereas the high-$\beta_{\parallel,e}$ population is located in regions of $\delta B_\parallel/B > 0$ (high-$\boldsymbol{B}$ strength). In this sense, we also conclude that in the case of electrons, the unstable population is located mainly in regions of low-$\boldsymbol{B}$ strength and high $\beta_{\parallel,e}$, where whistler waves are being excited, and the marginally stable population is located mainly in regions of high-$\boldsymbol{B}$ field and low $\beta_{\parallel,e}$. This also suggests that whistler waves interact with electrons so they move to regions of high-$\boldsymbol{B}$ strength. We will also see in Sections 3.5 and 3.6 that the electrons that contribute the most to the pressure anisotropy that destabilizes whistler waves are the ones that become trapped within mirror modes.

3.5. Physical Mechanism of Secondary IC/Whistler Excitation: Trapped and Passing Particles

In this section, we study the evolution of the ions and electrons that become trapped within mirror modes as part of the mirror instability's interaction with the particles. We characterize the pressure anisotropy and distribution functions of these populations at the moment of trapping, and provide evidence that they are able to destabilize parallel-propagating modes that ultimately allow them to escape the mirrors and regulate the overall anisotropy.

As part of their evolution, and after reaching secular growth, mirror modes start to trap particles of low parallel momentum $p_{\parallel,j}$ ($j = i$, e) in regions of low local magnetic field strength. The trapped particles bounce between these regions and conserve their magnetic moment in the process (Southwood & Kivelson 1993; Kunz et al. 2014). In order to investigate the relation between this trapping process and the excitation of these late IC and whistler waves, we select and track a population of ions and electrons throughout the evolution of the simulation, and study the trapped and passing (i.e., untrapped) subpopulations separately.

We select and track two populations of ions and two populations of electrons having relatively small and large parallel momentum at a particular time in the simulation. This way, we make sure that we can capture particles that eventually become trapped and others that remained passing. In our fiducial simulation b20m8w800, the two populations of ions that we track have parallel momentum of $-0.12 < p_{\parallel,i}/m_i c < 0.12$ and $0.3395 < p_{\parallel,i}/m_i c < 0.3405$ at $t \cdot s = 0.4$. Similarly, the two populations of electrons have $-0.2 < p_{\parallel,e}/m_e c < 0.2$ and $0.4599 < p_{\parallel,i}/m_i c < 0.4601$ at $t \cdot s = 0.4$.

In order to study the behavior of the tracked particles when the IC and whistler activity starts, we ask how many particles become trapped and how many become passing during the interval of time at which this activity happens, which we denote by $\Delta\tau_{\rm LR}$. To answer this, we look at Figure 2(g) and define $\Delta\tau_{\rm LR}$ as the interval of time of $0.52 < t \cdot s < 0.62$, which covers the exponential growth that δB_z^2 and $\delta B_{\perp,xy}^2$ undergo before saturating. This interval of time also covers the majority of the secular growth of mirror modes (see $\delta B_\parallel^2$).

Having this time interval well defined, we now must define the criterion by which we consider a particle to become trapped and passing during $\Delta\tau_{\rm LR}$, and for this, we look at the evolution of their parallel momentum. Similarly to Ley et al. (2023), we define a particle as trapped during $\Delta\tau_{\rm LR}$ if the median of its parallel momentum over $\Delta\tau_{\rm LR}$ is smaller than 1 standard deviation over $\Delta\tau_{\rm LR}$. We then define a particle as passing if the median of its parallel momentum over $\Delta\tau_{\rm LR}$ is greater than or equal to 1 standard deviation over $\Delta\tau_{\rm LR}$. This is a statement of small variation of $p_{\parallel,j}$ over $\Delta\tau_{\rm LR}$, which in turn is a proxy for an oscillatory behavior of $p_{\parallel,j}$, characteristic of a bouncing particle between mirror points. We confirm that this simple criterion gives excellent results in separating trapped from passing particles.

Figure 9 shows the evolution of the parallel momentum of a trapped and a passing ion (panels (a)) and a trapped and a passing electron (panel (b)), where the vertical gray-dashed lines indicate $\Delta\tau_{\rm LR}$. In Figure 9(a), we can see the the oscillation pattern in the evolution of the parallel momentum of the trapped ion during $\Delta\tau_{\rm LR}$ and until $t \cdot s \approx 0.7$, when it escapes. The parallel momentum of the passing ion evolves without major changes as the ion streams through the simulation box. This behavior is consistent with previous works using hybrid and fully kinetic simulations (Kunz et al. 2014; Riquelme et al. 2016).

In Figure 9(b), we can also see the oscillating pattern of the parallel momentum of the trapped electron, indicating bouncing inside mirror modes, which ends at $t \cdot s \approx 1.1$, when it escapes. The parallel momentum of the passing electron does not vary significantly during $\Delta\tau_{\rm LR}$, confirming that it was streaming along field lines at least at that interval.

It is worth noting, however, what happens after $\Delta\tau_{\rm LR}$. Our criterion for identifying particles as trapped and passing was only within $\Delta\tau_{\rm LR}$, and after that period of time particles can continue evolving into the saturated stage of mirror modes, where they can escape, be trapped again, or continue streaming unperturbed. Indeed, by looking at its parallel momentum, we

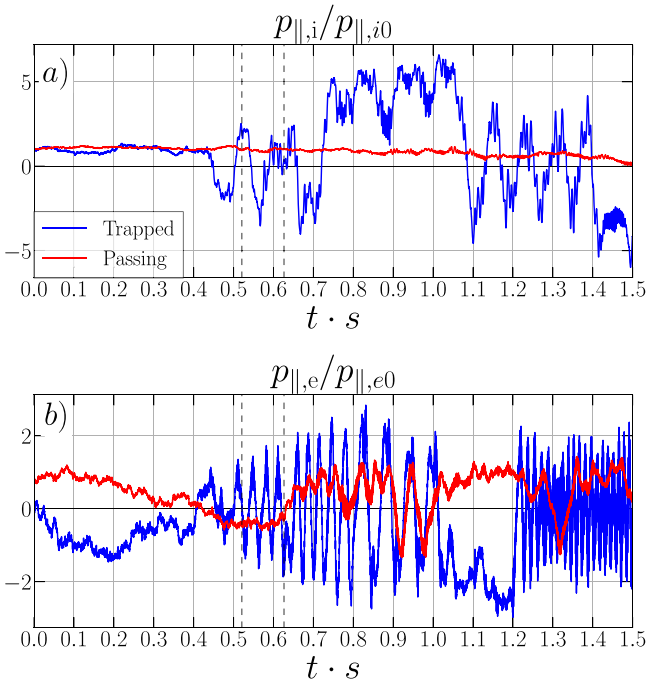

Figure 9. Panel (a): evolution of the parallel momentum of an individual trapped ion (blue line) and passing ion (red line) for our fiducial simulation b20m8w800. Panel (b): evolution of the parallel momentum of a trapped electron (blue line) and passing electron (red line) for run b20m8w800. The vertical gray-dashed lines in each panel indicate the time interval $\Delta\tau_{\mathrm{LR}}$.

can see that after escaping and streaming for a while, the trapped ion shown in Figure 9(a) gets trapped again at $t \cdot s \approx 1.1$, bounces inside a mirror mode and escapes again at $t \cdot s \approx 1.4$. Similarly, we can also see that the trapped electron shown in Figure 9(b) gets trapped again at $t \cdot s \approx 1.2$ and seems to stay trapped until the end of the simulation. Interestingly, the passing electron also gets trapped at around $t \cdot s \approx 0.7$, by looking at its parallel momentum, and then escapes again at $t \cdot s \approx 1.2$. Therefore, in a statistical sense, we can consider the particles as trapped and passing only over the particular period of time $\Delta\tau_{\mathrm{LR}}$ that we chose, after which they can continue evolving and turn into passing or trapped again, as long as the mirror saturation persists in the simulation.

3.6. Physical Mechanism of Secondary IC/Whistler Excitation: Distribution Functions

In this section, we look at the evolution of the pressure anisotropy and distribution functions of trapped and passing ions and electrons defined according to the criterion described in Section 3.5. We see that during $\Delta\tau_{\mathrm{LR}}$, both trapped ions and trapped electrons contribute most of the pressure anisotropy necessary to destabilize IC and whistler modes. We show that these IC and whistler waves interact in a quasilinear fashion with ions and electrons, respectively, and quickly regulate their pressure anisotropy such that their distributions evolve to a more isotropic state.

Figure 10(a) shows the evolution of the pressure anisotropy of trapped and passing ions. We can see that the anisotropy of trapped ions initially follows a double-adiabatic (CGL, blue-dotted line) evolution until $t \cdot s \approx 0.5$ (i.e., just starting $\Delta\tau_{\mathrm{LR}}$), when the mirror modes start to trap them. We can readily see that during $\Delta\tau_{\mathrm{LR}}$, the trapped ions develop a significant anisotropy, peaking at around $t \cdot s \approx 0.55$. The anisotropy is

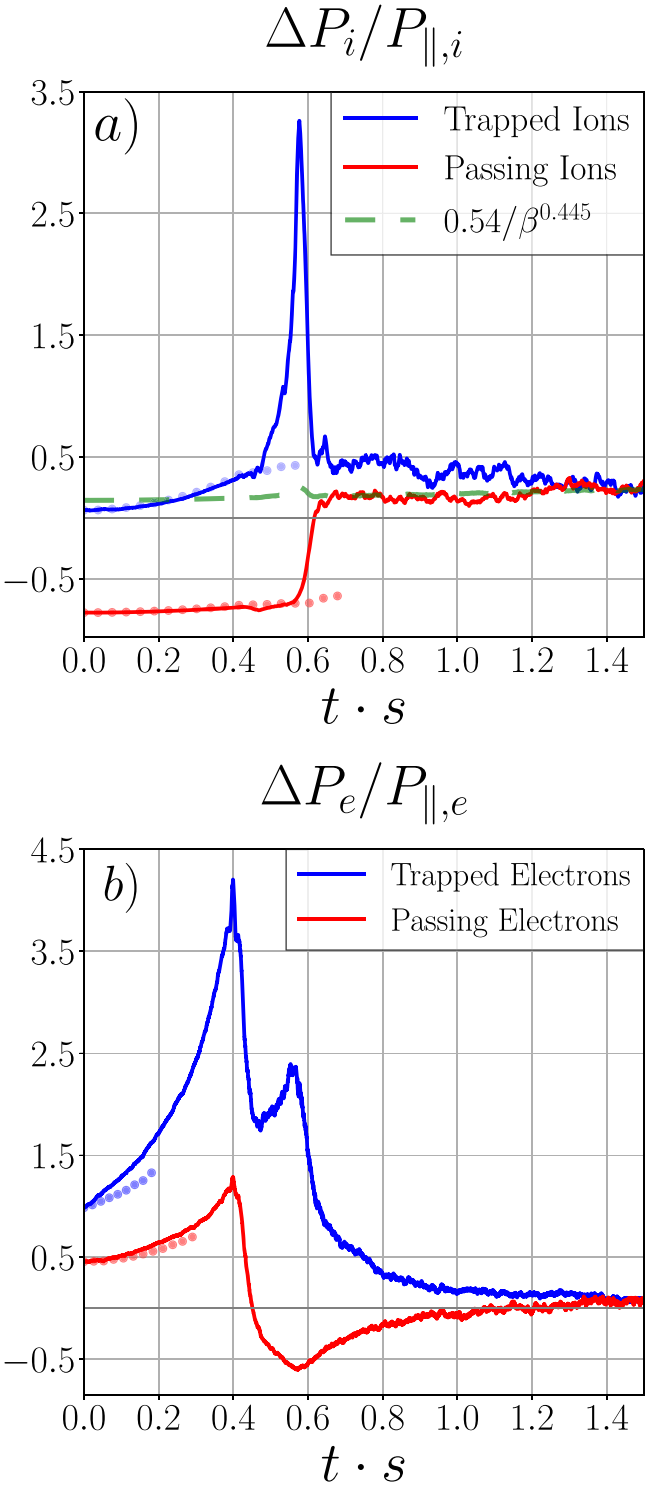

Figure 10. Panel (a): evolution of the pressure anisotropy of ions identified as trapped (blue line) and passing (red line) during $\Delta\tau_{\mathrm{LR}}$. The green-dashed line indicates the best-fit threshold to $\Delta P_{\parallel,i}/P_{\parallel,i}$ shown in Figure 3(a), and the dotted blue-gray and red lines show the corresponding double-adiabatic (CGL) evolution of trapped and passing ions, respectively. Panel (b): evolution of the pressure anisotropy of electrons identified as trapped (blue line) and passing (red line) during $\Delta\tau_{\mathrm{LR}}$. The dotted blue and red lines show the corresponding CGL evolution of trapped and passing electrons, respectively.

quickly regulated and converges to the best-fit threshold that we derived in Section 3.1 and show in Figure 3(a). Similarly, the pressure anisotropy of passing ions evolves in a relatively unperturbed fashion following CGL evolution (red-dotted line)

through the majority of $\Delta\tau_{\rm LR}$, until $t\cdot s\approx 0.6$, where it passes from negative values (consistent with passing ions having preferentially large parallel momentum) to a positive but, more isotropic state consistent with the best-fit threshold from Figure 3(a).

The behavior of the pressure anisotropy of trapped and passing particles can be understood as follows. Mirror modes interact resonantly with ions and electrons according to the resonance condition $\omega_M - k_{\parallel,M}v_\parallel = 0$, where ω_M and $k_{\parallel,M}$ are the frequency and parallel wavenumber of mirror modes, respectively, and $v_\parallel$ is the parallel velocity of the particle. The very low frequency of mirror modes, $\omega_M \sim 0$, implies that the resonant particles are the ones having very low $v_\parallel$ ($v_\parallel < \gamma_M/k_{\parallel,M}$, where γ_M is the mirror growth rate (Southwood & Kivelson 1993; Pokhotelov et al. 2002). These are the particles that become trapped within mirror modes (Kivelson & Southwood 1996). Consequently, all trapped particles have very low parallel velocity, and as a whole, they should naturally have a pressure anisotropy of $P_{\perp,j} > P_{\parallel,j}$ ($j = i,\ e$). Similarly, all passing particles have large $v_\parallel$, and therefore, they have a pressure anisotropy of $P_{\parallel,j} > P_{\perp,j}$. In this sense, Figure 10 is consistent with the trapping argument described in Kivelson & Southwood (1996) (see their Figure 1).

The fact that both trapped and passing ions evolve into the average level of ion anisotropy shown in Figure 3(a) shows that their trapped or passing condition corresponds to a transient state that passes after a time comparable to $\Delta\tau_{\rm LR}$. Also, notice that the anisotropy of the two populations (and for the whole population for that matter) is significant enough to drive IC waves unstable (see Section 3.3), and therefore, this can provide evidence for the source of the IC waves that we see. If this is the case, their interaction with ions is the source of the quick regulation of the anisotropy that we see in Figure 10(a). Interestingly, under this scenario, the regulation of the pressure anisotropy of passing ions, which happens at the same time as that of the trapped ions, should also be due to the interaction with these IC waves, meaning that the IC waves interact with both populations of trapped and passing ions simultaneously, and therefore, regulate the global ion anisotropy. We confirm that this is the case by looking at the evolution of the distribution functions of trapped and passing ions.

In the case of electrons, we observe a similar evolution in Figure 10(b). Initially, both trapped and passing electrons detach from their respective CGL evolution (blue- and red-dotted lines, respectively), and develop a significant anisotropy $\Delta P_e > 0$, that peaks at $t\cdot s\approx 0.4$. We also see that trapped electrons detach from their CGL evolution much earlier than passing electrons. This evolution then leads to the early burst of whistler waves, which also quickly regulates and drives anisotropies of both trapped and passing electrons toward a more isotropic state (see Section 3.2). As expected, the anisotropy of trapped electrons is higher than the one of the passing electrons. After this process, and during $\Delta\tau_{\rm LR}$, the anisotropy of trapped electrons increases again, while that of passing electrons continues to decrease. This way, we see that trapped electrons build up a pressure anisotropy $\Delta P_e > 0$ that is also quickly regulated after $\Delta\tau_{\rm LR}$, converging to an anisotropy level similar to the one of the general electron populations. The anisotropy $\Delta P_e < 0$ of the passing electrons also gets regulated toward a similar anisotropy level during the same time. This evolution of trapped electrons also suggests that they become anisotropic enough to destabilize whistler waves, and therefore, could be the source of the whistler activity observed at $t\cdot s > 0.6$.

It is worth noting that the evolution of $\delta B^2_{\perp,xy}$ and δB^2_z (see Figure 2(g)) at late stages shows that the cyclotron wave activity persists. It is then worth exploring whether the same trapping process described during $\Delta\tau_{\rm LR}$ is active during the saturated, nonlinear stage of the mirror instability, in addition to the already studied secular growth spanned by $\Delta\tau_{\rm LR}$. We will see that this is indeed the case.

We use the same sample of tracked ions and electrons as before, but we now define a new interval of time, $\Delta\tau_{\rm NL}$, to classify the particles as trapped and passing. Now let $\Delta\tau_{\rm NL}$ span the interval of $1.35 < t\cdot s < 1.45$, in order to match the time shown in the third column of Figure 8. We use the same criterion as before, namely, that a particle will be trapped/passing when the median of its parallel momentum over $\Delta\tau_{\rm NL}$ is smaller/greater than or equal to 1 standard deviation over $\Delta\tau_{\rm NL}$.

Figure 11 shows the evolution of the pressure anisotropy of trapped and passing ions (panel 11(a)) and trapped and passing electrons (panel 11(b)) identified during the interval $\Delta\tau_{\rm NL}$. In the case of the ions, we can see that the evolution of the pressure anisotropy of both trapped and passing ions follows a very similar trend throughout the linear phase of the mirror instability, and part of its secular growth as well. At $t\cdot s\approx 0.6$, the two curves start to separate from each other, and the pressure anisotropy of the passing ions starts to slightly decrease, whereas the pressure anisotropy of trapped ions sticks in the best-fit threshold until $t\cdot s\approx 1.0$, to then start to increase as it approaches $\Delta\tau_{\rm NL}$. Similar to the earlier interval $\Delta\tau_{\rm LR}$, the pressure anisotropy of passing ions decreases and reaches its minimum point at $t\cdot s\approx 1.4$, while the pressure anisotropy of trapped ions increases, and reaches its maximum point at around the same time. Note that the anisotropy peaks of both trapped and passing ions are now smaller than during $\Delta\tau_{\rm LR}$, but significant enough to still be able to excite IC waves, that then interact with the ions and regulate their pressure anisotropies. The smaller peaks can be due to a lower amount of free energy available in the system than at earlier times, as a significant amount of pitch-angle scattering has been undergone already.

In the case of electrons, a similar trend is observed. In Figure 11(b), the pressure anisotropy of both trapped (solid blue line) and passing (solid red line) electrons have a very similar initial behavior. They both respond similarly to the early whistler burst, to then separate their evolution around $t\cdot\approx 0.6$. At this point, the anisotropy of passing electrons starts to decrease, while the anisotropy of trapped electron increases. Again, the peak anisotropy of both trapped and passing electrons is reached at $t\cdot s\approx 1.4$, and peaks at a relatively smaller value than during $\Delta\tau_{\rm LR}$, but also significant enough to be able to excite whistler waves. These waves then interact with electrons and regulate their anisotropies, analogous to the ion case.

We can then conclude that even at later times, as long as there is enough free energy available in the system, the trapping process of both ions and electrons is able to contribute to the pressure anisotropy to excite IC and whistler waves, respectively, even at later stages. We argue that this process happens continuously, with different populations of particles undergoing trapping and untrapping processes at any specific interval of time during the late stages of the mirror instability.

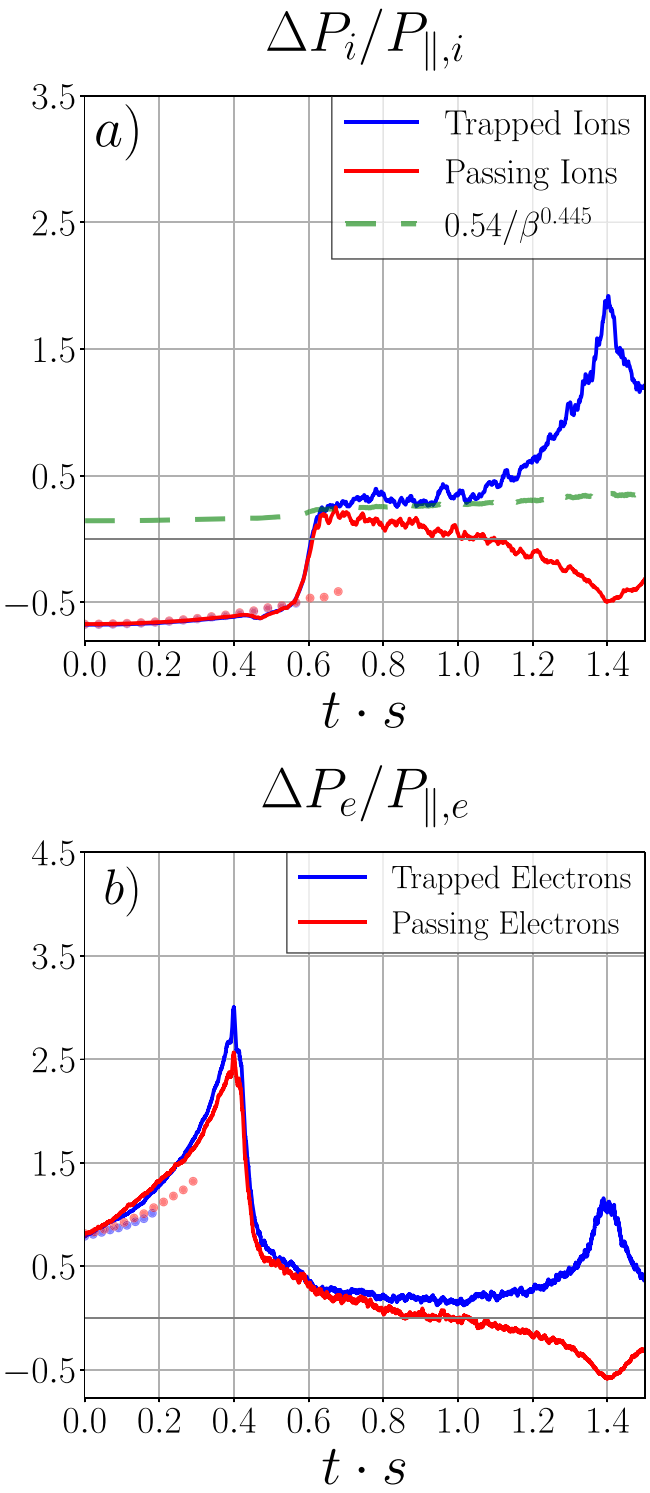

Figure 11. Panel (a): evolution of the pressure anisotropy of ions identified as trapped (blue line) and passing (red line) during $\Delta\tau_{\rm NL}$. The green-dashed line indicates the best-fit threshold to $\Delta P_{\parallel,i}/P_{\parallel,i}$ shown in Figure 3(a), and the dotted blue-gray and red lines show the corresponding double-adiabatic (CGL) evolution of trapped and passing ions, respectively. Panel (b): evolution of the pressure anisotropy of electrons identified as trapped (blue line) and passing (red line) during $\Delta\tau_{\rm NL}$. The blue- and red-dotted lines show the corresponding CGL evolution of trapped and passing electrons, respectively.

Figure 12 shows the distribution functions of trapped and passing ions and electrons at three different times, $t \cdot s = 0.57$, 0.61, and 0.75, spanning $\Delta\tau_{\rm LR}$ and also part of mirror's saturated stage. In the following, we describe the evolution of each population.

The distribution of trapped ions (Figures 12(a)–c)) shows a clear loss-cone-like form at $t \cdot s = 0.57$ (all outside the loss cone), meaning that all ions classified as trapped are effectively trapped in mirror troughs. At this time, trapped ions have reached their maximum pressure anisotropy according to Figure 10(a).

Once IC waves are excited, they interact with both trapped and passing ions via pitch-angle scattering in a quasilinear fashion (Kennel & Engelmann 1966). This diffusion process happens along paths of constant particle's energy in the frame moving with the waves (see, e.g., Squire et al. 2022):

$$v_{\perp,j}^2 + (v_{\parallel,j} - \omega/k_\parallel)^2 = \text{const.} \tag{5}$$

We plot these contours in solid white lines in each plot of Figure 12 as $v_{\perp,j}^2 + (v_{\parallel,j} - \omega/k_\parallel)^2 \approx v_{\perp,j}^2 + v_{\parallel,j}^2 = \text{const.}$, as in a high-$\beta$ scenario, the phase velocity of an IC wave offers a small correction of order $v_A/v_{th,i} = \sqrt{1/\beta}$. Additionally, the IC waves in our simulations are destabilized in both parallel and antiparallel directions to $\boldsymbol{B}$. We can see that the relaxation of the distribution function of trapped ions by the quasilinear interaction with IC waves agrees very well with these paths, by looking at $t \cdot s = 0.61$ and 0.75.

The distribution of passing ions (Figures 12 (d)–(f)) shows, on the one hand, a concentration of ions at low perpendicular velocities and relatively large parallel velocities, and it looks fairly symmetric in $v_\parallel$. This is consistent with having untrapped ions mainly streaming along the mean magnetic field in both directions. On the other hand, the population of large parallel velocity is also shown at $v_\parallel/c \approx 0.3$ (see Section 3.5). Interestingly, the passing ions also interact quasilinearly with IC waves, and this is particularly evident in the evolution of passing ions. Indeed, we can clearly see how the large parallel velocity population of passing ions evolves along the contours of constant particle energy with excellent agreement at $t \cdot s = 0.61$ and 0.75. We can understand the evolution of this population by looking at the gyroresonance condition

$$\omega - k_\parallel v_{\parallel,i} = \pm\omega_{c,i}. \tag{6}$$

If we look at the peak power at positive frequencies in the power spectrum shown in Figure 6(c), we can estimate the frequency and wavenumber at which most of the power of IC waves resides: $\omega/\omega_{c,i}^{\rm init} \approx 0.2$, and $ck_\parallel/\omega_{p,i}^{\rm init} \approx \pm 0.15$. From Equation (6) we can estimate then the parallel velocity of the ions interacting gyroresonantly with these IC waves:

$$\frac{v_{\parallel,i}}{c} = \frac{\omega/\omega_{c,i}^{\rm init} \mp 1}{(ck_\parallel/\omega_{p,i}^{\rm init})(m_i c^2/k_B T_i^{\rm init})^{1/2}(\beta_i^{\rm init}/2)^{1/2}}, \tag{7}$$

which gives $v_{\parallel,i}/c \approx 0.36$ and $v_\parallel/c \approx -0.24$, which falls in the range of the large parallel velocity population. The quasilinear evolution also happens with the population with a smaller parallel velocity.

The population of trapped electrons (Figures 12(g)–(i)) shows a very similar evolution to that of trapped ions; the loss-cone-like distribution is also apparent. The evolution of this distribution is also consistent with a quasilinear interaction now between the electron and whistler waves, driving the distribution toward isotropy along paths of constant particle energy, as can be seen at later times in Figure 12.

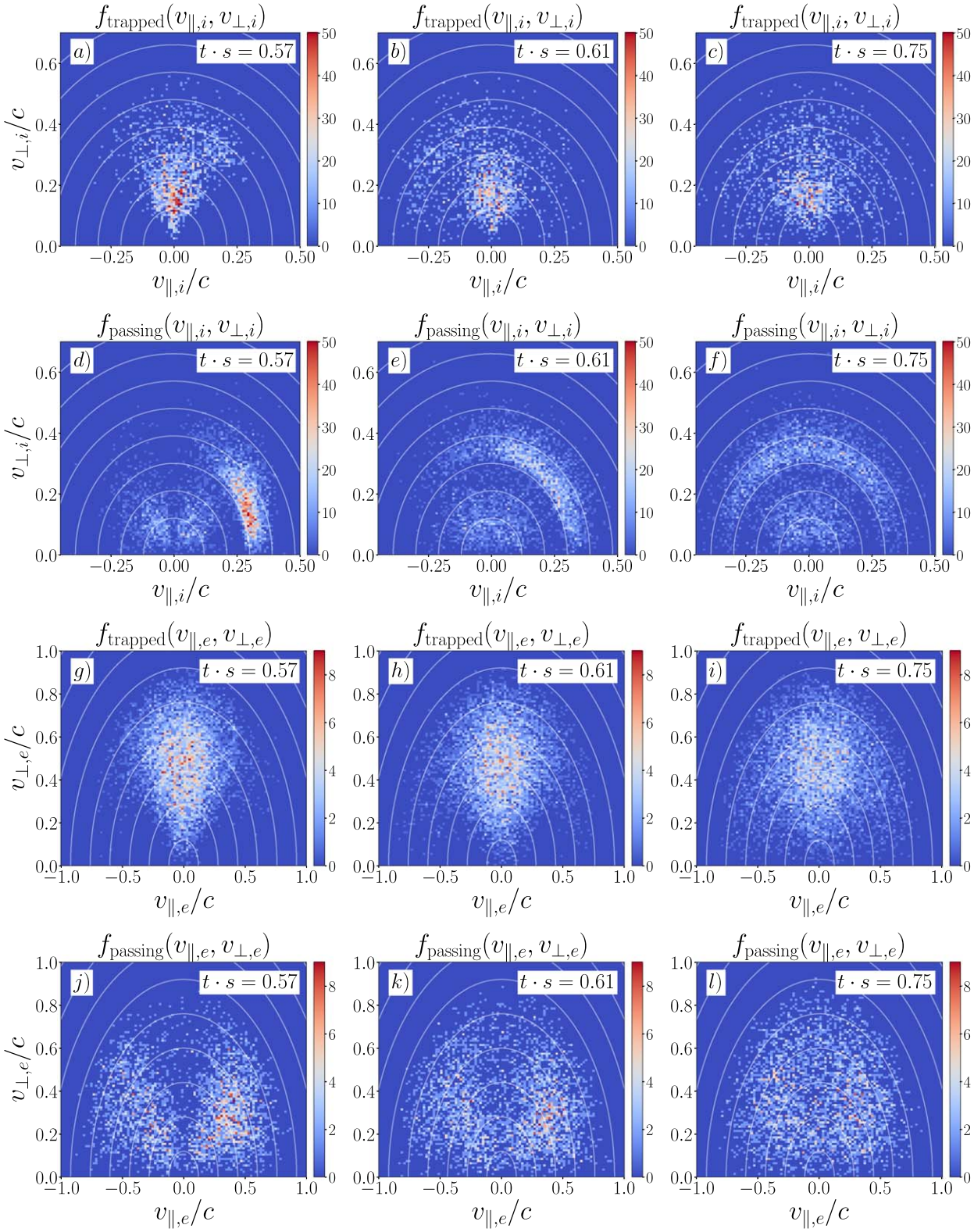

Figure 12. The distribution function $f(v_{\parallel,j}, v_{\perp,j})$ of trapped and passing ions and electrons at three different times: $t \cdot s = 0.57$ (first column starting from top), $t \cdot s = 0.61$ (second column), and $t \cdot s = 0.75$ (third column). The distribution function $f_{\rm trapped}(v_{\parallel,i}, v_{\perp,i})$ of the trapped ions is shown in the first row (starting from left), $f_{\rm passing}(v_{\parallel,i}, v_{\perp,i})$ for the passing ions are shown in the second row, $f_{\rm trapped}(v_{\parallel,e}, v_{\perp,e})$ for the trapped electrons are shown in the third row, and $f_{\rm passing}(v_{\parallel,e}, v_{\perp,e})$ for the passing electrons are shown in the fourth row. In all the plots, the solid white curves denote contours of constant particle energy in the frame moving with the waves: $v_{\perp,j}^2 + (v_{\parallel,j} - \omega/k_\parallel)^2 \approx v_{\perp,j}^2 + v_{\parallel,j}^2 = \text{const.}$ $(j = i, e)$. An animation is available in the HTML version of this paper. The animation shows the evolution throughout the simulation of the distribution of trapped ions and passing ions only (i.e., top two rows of the static figure) in the same format as shown in the static figure. The evolution runs from $t \cdot s = 0 - 1.5$.

(An animation of this figure is available.)

Finally, the population of passing electrons (Figures 12(j)–(l)) also shows a very similar evolution to that of the ions. The populated loss-cone shape of the distribution is also apparent, and we can see the quasilinear evolution of the distribution function along constant particle energy contours at later times.

We have shown that once ions and electrons get trapped in regions of low magnetic field strength of mirror modes, they get sufficiently anisotropic to destabilize parallel-propagating IC and whistler waves, respectively. During this process, both trapped ions and trapped electrons develop loss-cone-like distributions. Once excited, IC and whistler waves then interact with both populations of trapped and passing ions and electrons, respectively, in a quasilinear fashion, driving both populations of trapped and passing ions and electrons toward a more isotropic state. Consequently, this mechanism can contribute to regulating the global anisotropy of ions and electrons, and can thus be a pathway for particle escape and consequent saturation of mirror modes (Kunz et al. 2014).

It is worth mentioning, however, that the sample of tracked ions and electrons used to construct the trapped and passing populations constitute a small fraction of the entire distribution; moreover, the details about how ions and electrons can destabilize IC and whistler waves, respectively, involve the study of their entire distribution function, not only the trapped or the passing fractions. What we can state is that trapped ions and trapped electrons populations contribute most of the positive anisotropy necessary to destabilize parallel-propagating IC and whistler waves, respectively, but the destabilization of IC and whistler waves is produced by the combination of the passing and trapped ions and electrons, which, as a whole, do not obey loss-cone-like distributions.

In order to assess in more detail how the entire ion and electron distribution functions in our simulations are sufficiently unstable to IC and whistler waves, we can study the growth rate of anisotropy-driven, parallel-propagating, circularly polarized waves (e.g., Zweibel 2020)

$$\Gamma = \frac{\pi^2 e^2}{2}\frac{\omega_{c,j}^2}{\omega_{p,j}^2}\int p^2 dp d\mu v(1-\mu^2)\,\delta(\omega - kv\mu \pm \omega_c)A[f,\omega,k], \quad (8)$$

where $\omega_{p,j} = \sqrt{4\pi n/m_j}$ is the plasma frequency of species j ($j = i, e$), $\omega_{c,j} = eB/m_j c$ is the cyclotron frequency of species j, p is the particle momentum, $\mu = p_\parallel/p$ is the cosine of the pitch angle, and $A[f, \omega, k]$ is the anisotropy functional:

$$A[f,\omega,k] \equiv \frac{\partial f}{\partial p} + \left(\frac{kv}{\omega} - \mu\right)\frac{1}{p}\frac{\partial f}{\partial \mu}. \quad (9)$$

Instability is triggered when $A > 0$ in at least some region of phase space. In the case of the whistler instability, we can plug the whistler dispersion relation $\omega_W = \omega_{c,e}k_W^2 R_{L,e}^2/\beta_i$ into Equation (9) to obtain

$$A[f,\omega,k] \approx \frac{\partial f}{\partial p} + \left(\frac{v_{th,e}\beta_e}{\omega_{c,e}k_W R_{L,e}^2} - \mu\right)\frac{1}{p}\frac{\partial f}{\partial \mu}, \quad (10)$$

where we replaced the velocity $v \sim v_{th,e}$, as the distribution is mostly (but not entirely) thermal. Since the fastest growing mode for whistler waves has $k_W R_{L,e} \sim 1$, and $R_{L,e} = v_{th,e}/\omega_{c,e}$, we can simplify the above expression to

$$A[f,\omega,k] \approx \frac{\partial f}{\partial p} + (\beta_e - \mu)\frac{1}{p}\frac{\partial f}{\partial \mu} \approx \frac{\partial f}{\partial p} + \frac{\beta_e}{p}\frac{\partial f}{\partial \mu}, \quad (11)$$

as $\beta_e \gg 1$ in our case, so we can neglect the contribution of μ. Now, we can expand the distribution function in Legendre polynomials in μ (e.g., Zweibel 2020; Ley et al. 2023),

$$f_e(t,p,\mu) = \sum_{l=0}^{\infty} f_l(t,p)P_l(\mu), \quad (12)$$

where $f_l = \frac{2l+1}{2}\int_{-1}^{1} f_e(t,p,\mu)P_l(\mu)d\mu$. Expanding up to the P_2 term (where $P_2(\mu) = (3\mu^2 - 1)/2$ is the Legendre polynomial of order 2), $f(t,p,\mu) = f_0(t,p) + f_2(t,p)P_2(\mu)$ allows us to separate f into its isotropic and anisotropic parts, given the coupling of f_2 with the pressure anisotropy

$$\Delta P_e \equiv P_{\perp,e} - P_{\parallel,e} = -\frac{2}{5}\int p v f_2(t,p)p^2 dp. \quad (13)$$

Expanding $f(t, p, \mu)$ up to $P_2(\mu)$ in Equation (11), we get

$$A = \frac{\partial f_0}{\partial p} + \frac{\partial f_2}{\partial p}P_2(\mu) + 3\frac{\beta_e}{p}\mu f_2. \quad (14)$$

Assuming that the f_2 contribution is small (i.e., the deviations from a thermal distribution due to pressure anisotropy are small), the condition $A > 0$ implies

$$|f_2/f_0| \gtrsim \frac{1}{\beta_e}. \quad (15)$$

Therefore, we obtain the important result that, in a high-β plasma, the anisotropic part of the distribution, f_2, need only be a small fraction of the isotropic part f_0, of order $1/\beta_e$, to be able to excite whistler waves. For IC waves, as the dispersion relation is $\omega_{IC} = k_{IC}R_{L,i}/\sqrt{\beta_i}$, the condition reads

$$|f_2/f_0| \gtrsim \frac{1}{\sqrt{\beta_i}}. \quad (16)$$

Using these results, we can construct f_0 and f_2 from our PIC simulations and quantify the contribution of f_2 relative to f_0, going beyond the tracked particles from which we constructed the trapped and passing particles' distribution functions.

The first step consists of reconstructing $f_e(t, p, \mu)$ and $f_i(t, p, \mu)$. For this, we construct the histogram of a sample of 401,408 electrons in p_e and $\mu_e = p_{\parallel,e}/p_e$ and 401,408 ions in p_i and $\mu_i = p_{\parallel,i}/p_i$. In this sample, we do not distinguish between trapped and passing particles at any given time. This is shown in Figure 13 for $t \cdot s = 0.57$, at the onset of the IC/whistler activity.

We can see in Figure 13 that for both electrons (Figure 13(a)) and ions (Figure 13(b)), the distribution looks not very different from a thermal and isotropic distribution, with the most noticeable difference shown in μ. In the case of the ions, the distribution in μ_i looks more anisotropic than in the case of electrons, consistent with Figure 3. The departures from a thermal distribution will become more evident when we decompose $f_e(t, p, \mu)$ and $f_e(t, p, \mu)$ into their f_0 and f_2 Legendre decompositions.

We construct f_0 and f_2 from their definitions:

$$f_0 = \frac{1}{2}\int_{-1}^{1} f(t,p,\mu)P_0(\mu)d\mu = \frac{1}{2}\int_{-1}^{1} f(t,p,\mu)d\mu, \quad (17)$$

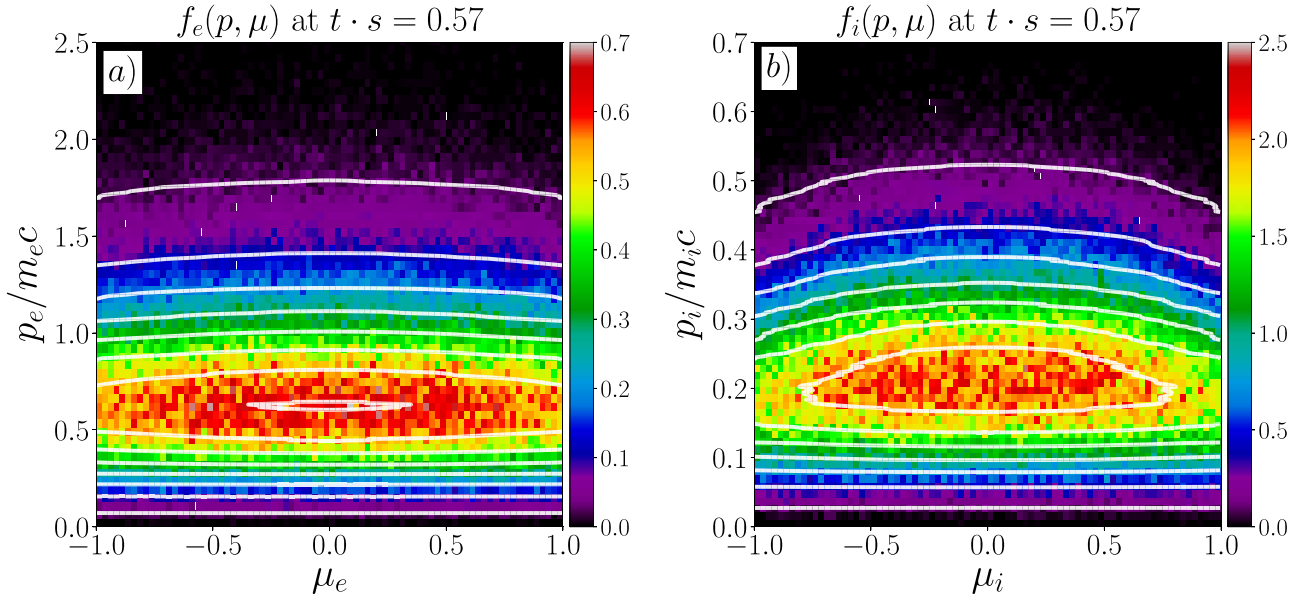

Figure 13. Panel (a): the distribution f_e of a sample of 401,408 electrons in p_e and μ_e at $t\cdot s = 0.57$. White contours show the reconstructed electron distribution function from f_0 and f_2: $f_e(t, p, \mu) \approx f_0(p_e) + f_2(p_e)P_2(\mu_e)$. Panel (b): the distribution f_i of a sample of 401,408 ions in p_i and μ_i at $t\cdot s = 0.57$. White contours show the reconstructed ion distribution function from its Legendre expansion f_0 and f_2: $f_i(t, p, \mu) \approx f_0(p_i) + f_2(p_i)P_2(\mu_i)$. The similarity between the white contours and the distribution reconstructed from the data shows that f is well represented by just the first two terms in the Legendre expansion.

$$f_2 = \frac{5}{2}\int_{-1}^{1} f(t, p, \mu)P_2(\mu)d\mu, \tag{18}$$

where $P_0(\mu) = 1$, $P_2(\mu) = (3\mu^2 - 1)/2$. We use $f_e(t, p, \mu)$ and $f_i(t, p, \mu)$ shown in Figure 13 to perform the integration. In order to obtain better statistics, we average over 50 snapshots around each time, and the shaded regions show 1 standard deviation around the mean value. The results are shown in Figure 14 at $t\cdot s = 0.57$.

We can see that there is a small but finite f_2 contribution for both ion and electron distribution functions. Moreover, the estimation shown in Figure 14 shows that at $t\cdot s = 0.57$ the ratio $|f_2(p_e)/f_0(p_e)|$ for electrons is comparable to or larger than $1/\beta_e$, and for the ions $|f_2(p_i)/f_0(p_i)|$ is also comparable to or larger than $1/\sqrt{\beta_i}$. Therefore, the distribution function as a whole has an f_2 contribution that even when it is smaller than the isotropic part f_0, it is nonetheless large enough to destabilize both whistlers and IC waves at $t\cdot s = 0.57$, given the high values of β_e,β_i. Recent works have emphasized this argument in great detail (Bott et al. 2023).

Finally, we validate our Legendre decomposition procedure and truncation up to the P_2 term by two means. First, we reconstruct the distribution function of both ions and electrons using only their f_0 and f_2 terms, $f_e(t, p, \mu) \approx f_0(p_e) + f_2(p_e)P_2(\mu_e)$ and $f_i(t, p, \mu) \approx f_0(p_i) + f_2(p_i)P_2(\mu_i)$. We show this in Figure 13 at $t\cdot s = 0.57$ as white contours. We can see that the reconstructed distribution functions are consistent with the full distributions of both ions and electrons, meaning that we are able to capture the main features of the distributions with just the first two terms of the Legendre expansion. Second, we calculate the ion and electron pressure anisotropy using Equation (13) and compare them with the pressure anisotropy shown in Figure 3. This is shown in the Appendix, and we obtain very good agreement.

4. Mass Ratio Dependence

In this section, we compare simulations with different mass ratios: $m_i/m_e = 8$, $m_i/m_e = 32$, and $m_i/m_e = 64$, but with the same initial conditions for ions, as shown for runs b20m8w800, b20m32w800,and b20m64w800 in Table 1, although with somewhat different temperatures. We see that IC and whistler waves' signatures do appear in all three simulations, and thus, they do not seem to present a strong dependence on mass ratio.

Figure 15 shows the evolution of $\delta B_\parallel^2$ (panel (a)) and δB_z^2 (panel (b)) for the three runs with mass ratios: $m_i/m_e = 8$, 32, and 64 (runs b20m8w800, b20m32w800, and b20m64w800 in Table 1). We can see a very consistent evolution of $\delta B_\parallel^2$ in all three runs, meaning that m_i/m_e does not play a significant role in the early evolution and saturation of the mirror instability. Similarly, δB_z^2 shows the same features in all three runs, especially during mirrors' secular growth and saturated stages ($t\cdot s \approx 0.5$ onward). The early peak in δB_z^2 at $t\cdot s \approx 0.4$ corresponding to the early whistler burst is also seen in the three runs, but more prominently in the simulation with $m_i/m_e = 8$. This is possibly due to an enhancement of this wave activity by the ions, which are able to weakly feel the presence of whistlers, as the mass separation is not very large. This effect disappears as the mass ratio increases, and the early whistlers only affect the electrons. More importantly, for $t\cdot s > 0.5$, all three runs show a very similar evolution of δB_z^2.

Figure 16 shows the evolution of the pressure anisotropy of ions (panel (a)) and electrons (panel (b)) for the same three runs. In the case of the ions, we can see an overall evolution that is very consistent in all three runs, both in the early and late stages. We can see a smaller anisotropy overshoot for the simulation with $m_i/m_e = 8$ at $t\cdot s \approx 0.4$, coincident with the enhancement seen in δB_z^2, during the early whistler burst, suggesting that ions can weakly interact with the whistlers at this mass ratio, and consequently their anisotropy does not reach the same overshoot as the rest of the runs.

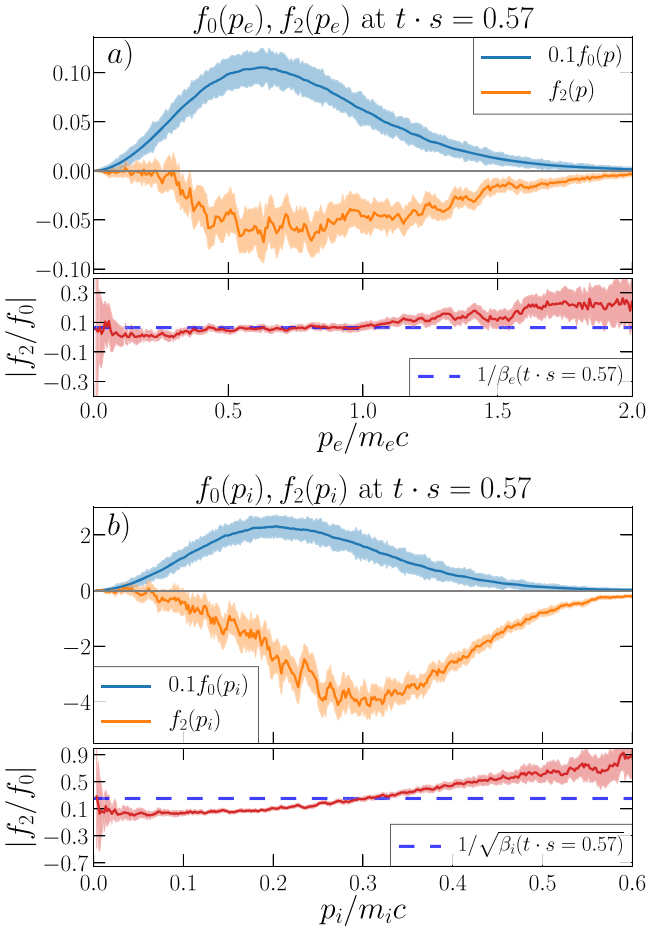

Figure 14. Panel (a): the first two terms in the Legendre expansion of the electron distribution function $f_e(t, p, \mu)$: $f_0(p_e)$ (blue line), and $f_2(p_e)$ (orange line) at $t \cdot s = 0.57$. Both f_0 and f_2 are averaged over 50 adjacent snapshots (equivalent to $\Delta t \cdot s \approx 0.03$). f_0 is multiplied by 0.1 for better visualization. The shaded regions represent 1 standard deviation around the mean. The lower plot shows the ratio f_2/f_0 (solid red line), and the red-shaded region represents one standard deviation around its mean. The solid blue line represents the value of $1/\beta_e$ at $t \cdot s = 0.57$. Panel (b): $f_0(p_i)$ (blue line), and $f_2(p_i)$ (orange line) from the Legendre expansion of $f_i(t, p, \mu)$ at $t \cdot s = 0.57$, averaged over 50 adjacent snapshots. f_0 is multiplied by 0.1 for better visualization. Shaded regions represent 1 standard deviation around the mean. The lower plot shows the ratio f_2/f_0 (solid red line), and the red-shaded region represents 1 standard deviation around its mean. The solid blue line represents the value of $1/\sqrt{\beta_i}$ at $t \cdot s = 0.57$.

Notwithstanding the foregoing, we can see how all three runs display a very similar pressure anisotropy evolution afterward, which is also well described by the best-fit threshold $\Delta P_i \propto \beta_i^{-0.45}$ shown in Figure 3.

In the case of the electron pressure anisotropy ΔP_e, we can also see a similar evolution overall in Figure 16(b). The overshoot at $t \cdot s \approx 0.4$ is larger for decreasing mass ratios, possibly due to the fact that the whistler amplitude required for efficient scattering decreases as m_i/m_e increases, as explained above. This means that, after $\Delta P_e/P_{e,\parallel}$ has surpassed the threshold for efficient growth of the whistler modes, the simulations with larger m_i/m_e take shorter times to reach the necessary whistler amplitude to efficiently scatter the electrons. This implies that the overshoot decreases for higher mass ratios. During late stages, we can see a very similar evolution of ΔP_e in all three runs, which is even more evident for

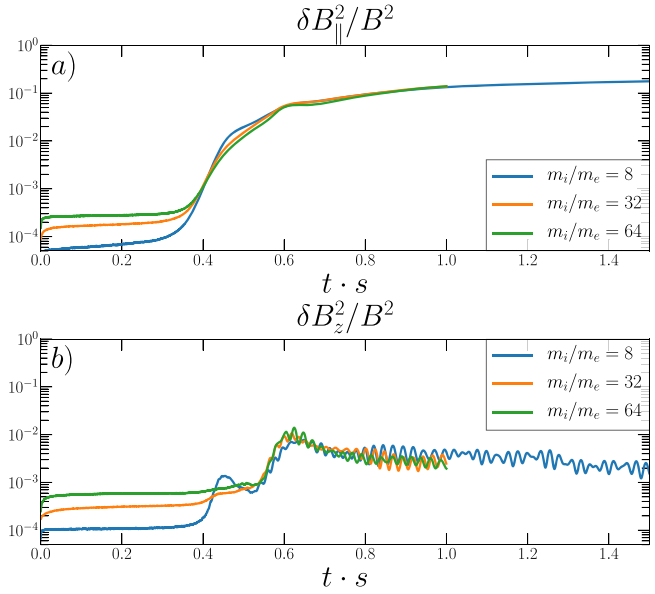

Figure 15. Panel (a): the energy in $\delta B_\parallel$, the parallel component of the magnetic field fluctuations $\delta \boldsymbol{B}$, for three simulations with different mass ratios: $m_i/m_e = 8$ (run b20m8w8, blue line), $m_i/m_e = 32$ (run b20m32w8, orange line), and $m_i/m_e = 64$ (run b20m64w8, green line). Panel (b): the energy in δB_z, the perpendicular component of $\delta \boldsymbol{B}$ out of the plane of the simulation in the same runs.

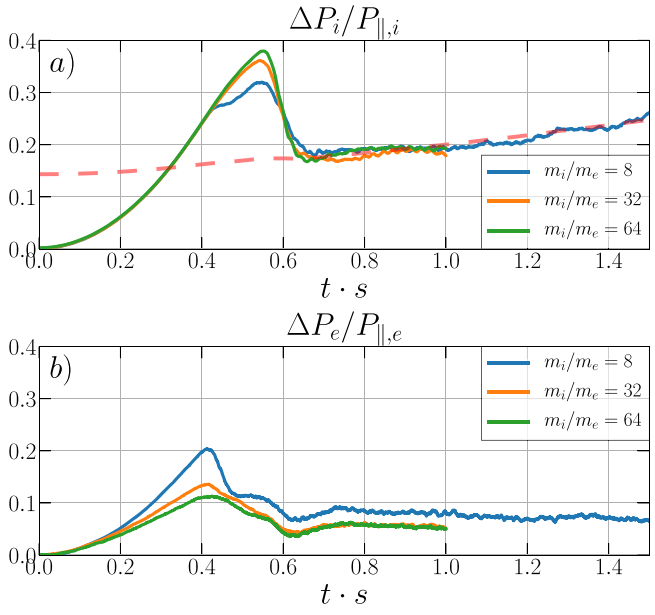

Figure 16. Panel (a): evolution of the ion pressure anisotropy for three simulations with different mass ratios: $m_i/m_e = 8$ (run b20m8w8, blue line), $m_i/m_e = 32$ (run b20m32w8, orange line), and $m_i/m_e = 64$ (run b20m64w8, green line). The red-dashed line indicates the best fit of the threshold shown in Figure 3(a), $\Delta P_i/P_{\parallel,i} \propto \beta_{\parallel,i}^{-0.45}$. Panel (b): same as in panel a but for the electron pressure anisotropy in the same runs.

$m_i/m_e = 32$ and 64 (orange and green curves in Figure 16(a)), which essentially lie on top of each other.

Finally, Figure 17 shows the power spectrum of $\delta B_z(\omega, k_\parallel) + i\delta B_{\perp,xy}(\omega, k_\parallel)$ for the simulation with $m_i/m_e = 32$ (Figure 17(a)) and with $m_i/m_e = 64$ (Figure 17(b)). Here we also see a very similar power distribution at both mass ratios, showing both left-handed and right-handed polarized waves (positive and negative frequencies, respectively). The peak

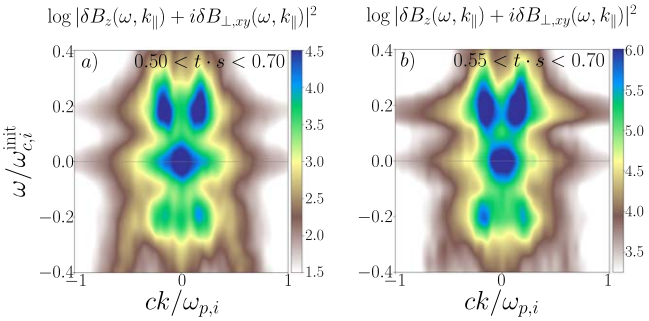

Figure 17. The power spectrum of $\delta B_z(\omega, k_\parallel) + i\delta B_\perp(\omega, k_\parallel)$ at $0.5 < t \cdot s < 0.7$ for $m_i/m_e = 32$ (run b20m32w800, left panel) and $m_i/m_e = 64$ (run b20m64w800, right panel). Positive and negative frequencies show the power in left-handed and right-handed polarized waves, respectively. Note that the color bar range is different for each figure.

power is also observed at the same frequencies and wavenumbers as in Figure 6 for both polarizations.

This way, we can see that the linear and nonlinear evolution of the mirror instability and the late IC and whistler evolution are well captured in our simulations, and it does not strongly depend on mass ratio.

5. Dependence on Initial Plasma β

We tested whether the IC and whistler waves' activity is present in simulations with $\beta_i^{\rm init} = 2$ (i.e., total $\beta^{\rm init} = 4$), and $\beta_i^{\rm init} = 40$ (i.e., total $\beta^{\rm init} = 80$), and compare them with our fiducial simulation at $\beta_i^{\rm init} = 20$. We confirm that the mirror instability can develop in all simulations, and both IC and whistler waves do appear at nonlinear stages.

The power spectrum of $\delta B_z(\omega, k_\parallel) + i\delta B_{\perp,xy}(\omega, k_\parallel)$ is shown in Figure 18 for the three runs with different initial $\beta_i^{\rm init}$, and we can see that it is similar among the three $\beta_i^{\rm init}$ cases. In all three cases, we see the power concentrated at $\omega \sim 0$ corresponding to mirror modes. In addition, we also see a concentration of power in right and left polarized waves, so both IC and whistler waves are also present, although their peak frequency changes. For the $\beta_i^{\rm init} = 2$ case, we see that the peak frequency is at $\omega/\omega_{c,i}^{\rm init} \approx 0.5$, whereas in the $\beta_i^{\rm init} = 40$ case, it shifts to smaller values, $\omega/\omega_{c,i}^{\rm init} \approx 0.1$. This shift in peak frequency can also be explained by the IC and whistler dispersion relations analogous to our discussion in Section 3.3.

Figure 19 compares the evolutions of $\delta B_\parallel^2$ (i.e., mainly the development of the mirror instability, panel (a)) and of δB_z^2 (i.e., the secondary IC and whistlers, panel (b)) for the three runs with different initial $\beta_i^{\rm init}$ (the other physical parameters are the same, see Table 1). In all three cases, we can see an exponential phase followed by the secular and saturated stages characteristic of the mirror instability, which develops earlier for higher initial $\beta^{\rm init}$, consistent with the smaller anisotropy threshold for the growth of the mirror instability at larger beta. The amplitude of $\delta B_\parallel^2$ at the saturated stage is comparable for both the $\beta^{\rm init} = 20$ and 40 runs, and is smaller for the $\beta^{\rm init} = 2$ run, as also seen by previous works (e.g., Riquelme et al. 2015).

When we look at the evolution of δB_z^2 in Figure 19(b), we can see that for both the $\beta^{\rm init} = 20$ and 40 runs, the evolution is similar: both display an early whistler burst at $t \cdot s \approx 0.4$, and an IC/whistler excitation stage ($t \cdot s \approx 0.5$ onward) at almost the same amplitude. In the case of the $\beta^{\rm init} = 2$ run, we can see that the first exponential growth in δB_z^2 at $t \cdot s \approx 0.6$ is consistent with an IC burst (see, e.g., Ley et al. 2019), after which we see the typical oscillation pattern that the excitation of late IC and whistler waves produces, from $t \cdot s \approx 0.8$ onward, saturating at an amplitude similar to that of the rest of the runs, and displaying a very high-frequency oscillation.

In Figure 20, we compare the evolution of the ion and electron pressure anisotropy plotted as a function of their parallel plasma β_i for the three simulations with different initial β_i. (As in all our simulations the mean magnetic field strength is continuously increasing, so the particles' β_i decreases over time, and therefore, the simulation evolves toward the left in Figure 20.)

In the case of the ions (Figure 20(a)), we can see a similar overshoot and subsequent regulation, but the overshoot occurs at a lower anisotropy value for increasing β_i. This is consistent with the inverse β_i dependence of the mirror instability threshold: mirror modes are excited earlier at higher β_i, and therefore have relatively more time to regulate the anisotropy before it reaches a higher overshoot. Interestingly, the saturated stage of the ion pressure anisotropy is consistent with the theoretical IC threshold from Gary & Lee (1994): $\Delta P_i/P_{\parallel,i} = 0.53\beta_{\parallel,i}^{-0.40}$ for $\gamma_{\rm IC}/\omega_{c,i} = 10^{-2}$ (see Figure 3(a)) in all three runs, suggesting a universality in the threshold that $\Delta P_i/P_{\parallel,i}$ follows, as a consequence of the excitation of IC waves during mirrors' saturated stage. (In the case of the $\beta_i^{\rm init} = 40$ run, however, it is more unclear whether it can follow the abovementioned threshold at late stages, given the short duration of this run.)

In the case of electrons (Figure 20(b)), we can also see that the overshoot is reached at lower values of the pressure anisotropy $\Delta P_e/P_{\parallel,e}$ for increasing initial beta, consistent with an inverse-β_i dependence now of the whistler instability anisotropy threshold. It is interesting to note that after the anisotropy overshoot, and during these late stages, the electron pressure anisotropy tends to be significantly smaller than the expectation from the threshold for the whistler instability in the higher initial β_i runs ($\beta_i^{\rm init} = 20$ and 40), irrespective of the generation of pressure anisotropy that the continuous amplification of the magnetic field produces as a consequence of the shear motion in the simulation. Notice, however, that in low magnetic field regions, the electron pressure anisotropy is larger than the whistler threshold, and therefore, enough to excite whistlers (Figure 8). This shows the key role played by mirror-generated magnetic troughs in creating the conditions to excite whistlers despite the fact that, globally, the pressure anisotropy may not be enough to make these waves unstable. On the other hand, in the $\beta_i^{\rm init} = 2$ run, $\Delta P_e/P_{\parallel,e}$ continues to weakly grow because of the continuous B amplification, and this is done following a marginal stability state well described by the threshold of the whistler instability of $\Delta P_e/P_{\parallel,e} \propto \beta^{-0.55}$ (Gary & Wang 1996), consistent with previous works at lower $\beta_{\parallel,e}$ (Ahmadi et al. 2018).

The persistence of the late IC and whistler activity at different initial plasma β_i suggests that this phenomenon is a natural consequence of the excitation of the mirror instability. In other words, in a weakly collisional plasma with an initial ion plasma β_i sufficiently high to effectively excite the mirror instability, the excitation of IC and whistler waves at its late, saturated stages seems to be ubiquitous.

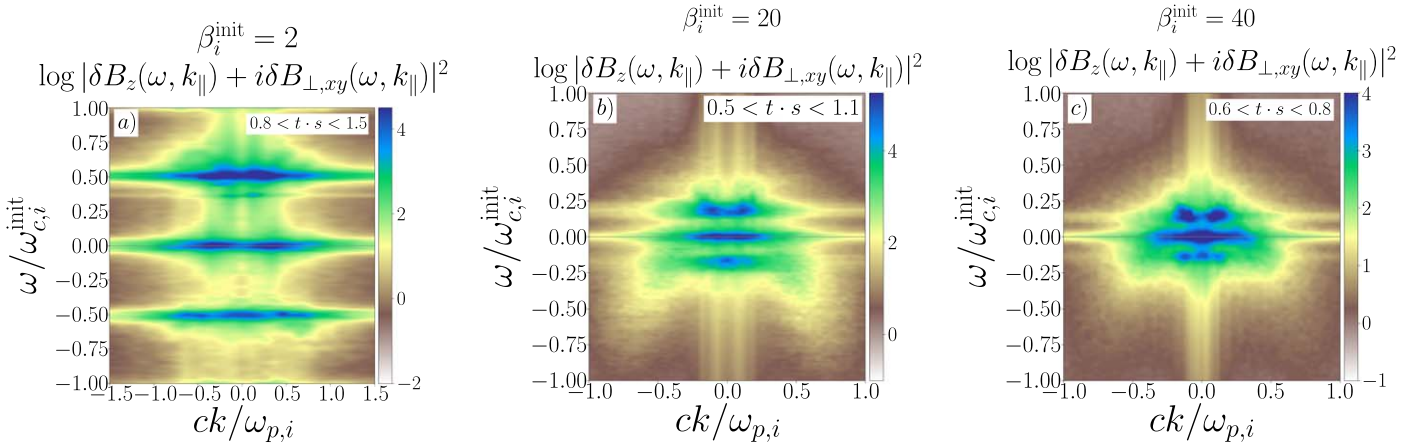

Figure 18. The power spectrum of $\delta B_z(\omega, k_\parallel) + i\delta B_{\perp,xy}(\omega, k_\parallel)$ for three runs with different initial ion beta: $\beta_i^{\rm init} = 2$ (panel (a), run b2m8w800), $\beta_i^{\rm init} = 20$ (panel (b), run b20m8w800), and $\beta_i^{\rm init} = 40$ (panel (c), run b40m8w800). Positive and negative frequencies show the power in left-handed and right-handed polarized waves, respectively.

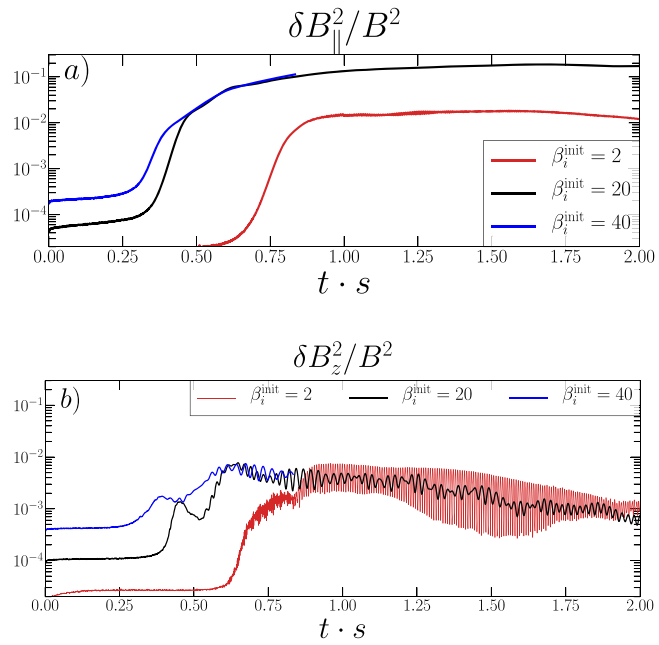

Figure 19. Panel (a): evolution of $\delta B_\parallel^2$ for three simulations with different initial ion beta: $\beta_i^{\rm init} = 2$ (solid red line, run b2m8w800), $\beta_i^{\rm init} = 20$ (solid black line, run b20m8w800), and $\beta_i^{\rm init} = 40$ (solid blue line, run b40m8w800). Panel (b): evolution of δB_z^2 for the same three simulations shown in panel (a).

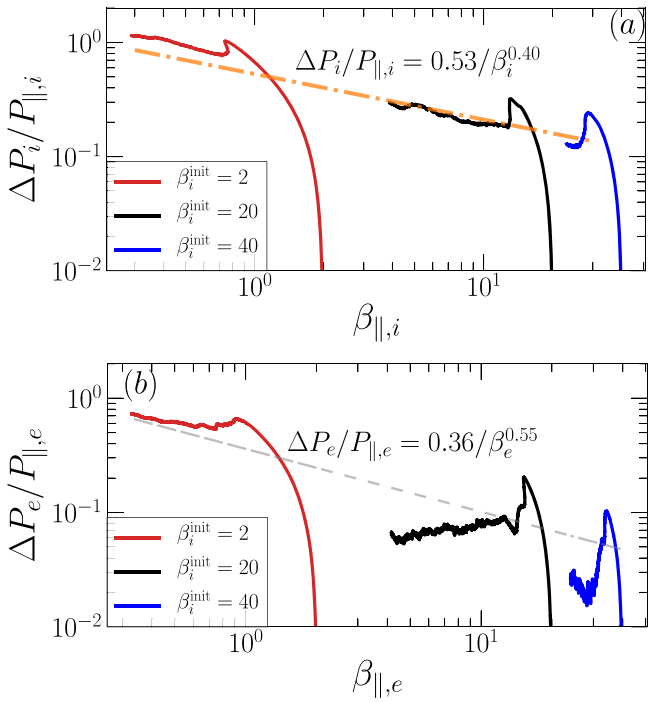

Figure 20. Panel (a): ion anisotropy $\Delta P_i/P_{\parallel,i}$ as a function of parallel ion beta, $\beta_{\parallel,i}$ (with respect to the main magnetic field $\boldsymbol{B}$) for three different simulations with different initial ion beta: $\beta_i^{\rm init} = 2$ (solid red line, run b2m8w800), $\beta_i^{\rm init} = 20$ (solid black line, run b20m8w800), and $\beta_i^{\rm init} = 40$ (solid blue line, run b40m8w800). The orange-dashed–dotted line shows the IC threshold of $\Delta P_i/P_{\parallel,i} = 0.53/\beta_{\parallel,i}^{0.4}$ from Gary & Lee (1994) for $\gamma_{\rm IC}/\omega_{c,i} = 10^{-2}$. Panel (b): electron anisotropy $\Delta P_e/P_{\parallel,e}$ as a function of parallel electron beta, $\beta_{\parallel,e}$ for the same three simulations shown in panel (a). The gray-dashed line in this case shows the threshold for the whistler instability, $\Delta P_e/P_{\parallel,e} = 0.36\beta_{\parallel,e}^{-0.55}$ for the growth rate of $\gamma = 0.01\omega_{c,e}$ from Gary & Wang (1996).

6. Summary and Discussion

In summary, we have performed fully kinetic PIC simulations of a collisionless plasma subject to a continuous amplification of the background magnetic field to study the nonlinear stages of the mirror instability and the ensuing excitation of secondary IC and whistler instabilities, in conditions where plasma pressure dominates over magnetic pressure (high β). After mirror modes reach high amplitudes and are able to trap ions and electrons within regions of low $\boldsymbol{B}$, we observe the excitation of subdominant left-handed polarized IC and right-handed polarized whistler waves that persist throughout the rest of the simulation, well into the nonlinear stages of the mirror instability (see Section 3.3). The whistler waves in our simulations seem to be consistent with the observations of whistler lion roars in lower-β environments of the Earth's magnetosheath.

By tracking ions and electrons through the simulation, we studied the excitation mechanism of both IC and whistler waves. We characterized the population of tracked particles as trapped and passing (i.e., untrapped) within mirror modes, and followed the evolution of their distribution functions. We observed that the trapped population of both ions and electrons becomes highly anisotropic while trapped inside mirror modes,

contributing most of the anisotropy that allows the plasma to become unstable to IC and whistler waves, respectively. On the other hand, the passing ions and electrons developed features concentrated at small perpendicular and large parallel velocities, and fairly symmetric with respect to $v_\parallel$, with a clear absence at small parallel velocities (see Section 3.6).

Once IC and whistlers are excited, they interact with both trapped and passing populations of ions and electrons, respectively, via gyroresonant pitch-angle scattering. As a result of this interaction, both trapped ions and electrons reduce their anisotropy and escape from magnetic troughs of mirror modes, following the prediction of quasilinear theory. The passing ion and electron populations evolve in a similar manner (see Figure 12). Interestingly, this process is observed to regulate the global anisotropy of ions and electrons in the simulation, driving the ion pressure anisotropy toward the IC instability threshold (Gary & Lee 1994), and the electron pressure anisotropy toward a global anisotropy much smaller than expected from the theoretical whistler threshold. Given this low electron pressure anisotropy, the whistler excitation can be explained by the fact that, within mirror-generated magnetic troughs, the pressure anisotropy is locally larger than the whistler threshold (Figure 8(i)). Thus, we interpret the whistler-driven regulation of electron pressure anisotropy as a local phenomenon, mainly produced by trapped electrons within nonlinear mirror structures.

The excitation of the secondary IC and whistler waves is maintained as long as mirror modes are present and growing, even at late stages where mirror modes have become highly nonlinear. This was also observed in simulations of lower and higher initial plasma β. This way, IC and whistler waves could be a concomitant feature of the nonlinear evolution of the mirror instability, and provide an interesting physical connection between ion-scale instabilities and electron-scale physics.

In this work, we did not vary the scale separation ratio $\omega_{c,i}/s$. In an environment like the ICM, turbulent eddies could drive the plasma locally through shear motions at kinetic scales with a wide range of frequencies s, and we typically expect larger kinetic energy at low frequencies (i.e., higher $\omega_{c,i}/s$). For larger values of $\omega_{c,i}/s$, previous works have shown that mirror modes can develop comparatively earlier in the simulations, therefore, having relatively more time to saturate, and reaching similar amplitudes (Kunz et al. 2014; Melville et al. 2016; Riquelme et al. 2016; Ley et al. 2023). In this sense, we would expect a similar late excitation of IC and whistler waves once mirror modes have reached a saturated stage.

The excitation of IC and whistler waves at saturated stages of the mirror instability modulates its nonlinear evolution, and therefore, could affect transport processes in the ICM in which mirror modes come into play.

Particularly important is the pressure anisotropy regulation in the context of collisionless heating and dissipation via magnetic pumping in the ICM (Kunz et al. 2011; Ley et al. 2023). The marginal stability level that the ion pressure anisotropy reaches the saturated stage, $\Delta P_i \propto \beta_{\parallel,i}^{0.45}$ (see Figure 3(a), also correctly pointed out by Sironi & Narayan 2015) is larger than the usual mirror threshold $1/\beta_{\parallel,i}$ by a factor of $\sim\beta_{\parallel,i}^{0.55}$, which directly translates into an excess heating of the same order. Indeed, given that β is estimated to be $\beta \sim 10$–100 in the ICM, and that the heating rate is directly proportional to the pressure anisotropy, this could imply a heating rate several times larger than predicted from the mirror threshold, enhancing the efficiency of the mechanism by draining more energy from the turbulent motions that drive the pumping.

The structures of high and low magnetic fields that mirror modes produce in the saturated stage seem to be persistent in time, and its energy $\delta B_\parallel^2$ does not decrease as long as the amplification of the mean magnetic field $\boldsymbol{B}$ is maintained (see Figure 2(g)). Even when this amplification is halted or reversed, the decaying timescales of mirror modes are large compared to the typical ion gyroperiod (Melville et al. 2016; Ley et al. 2023). This implies that the trapping process of ions and electrons also persists, along with the excitation of secondary IC and whistlers. This source of whistler waves can have interesting implications in the context of ICM thermal conduction models like whistler-regulated MHD (Drake et al. 2021), as they can dominate the electron scattering in the presence of mirror modes.

This source of whistler waves associated with mirror modes can also influence the suppression of the effective heat conductivity in the plasma even in the absence of heat fluxes (Komarov et al. 2016; Riquelme et al. 2016; Roberg-Clark et al. 2016, 2018), and this can have consequences in larger-scale instabilities such as the magneto-thermal instability (Balbus 2000; Berlok et al. 2021; Perrone & Latter 2022a, 2022b).

Future work aimed toward 3D fully kinetic PIC simulations would be required to have a full understanding of the consequences of the mirror instability and secondary IC/whistler excitation in these high-β plasmas.

Acknowledgments

The authors thank the anonymous referee for the insightful comments and suggestions that improved the paper. We thank Aaron Tran for providing the dispersion solver used in this work, and we thank Lorenzo Sironi, Jonathan Squire, and Alexander Schekochihin for useful comments and discussion. F.L. acknowledges support from NSF grant No. PHY-2010189. M.R. thanks support from ANID Fondecyt Regular grant No. 1191673. This work used the Extreme Science and Engineering Discovery Environment (XSEDE), which is supported by National Science Foundation grant No. ACI-1548562. This work used the XSEDE supercomputer Stampede2 at the Texas Advanced Computer Center (TACC) through allocation TG-AST190019 (Towns et al. 2014). This research was performed using the computing resources and assistance of the UW-Madison Center For High Throughput Computing (CHTC) in the Department of Computer Sciences. This research was partially supported by the supercomputing infrastructure of the NLHPC (ECM-02).

Appendix
Pressure Anisotropy Evolution from Legendre Decomposition

The expansion of the electron distribution $f_e(t, p, \mu)$ and ion distribution $f_i(t, p, \mu)$ in Section 3.6 was truncated at the $P_2(\mu)$ term, as we are interested in the coupling that the $f_2(p)$ has with the pressure anisotropy

$$\Delta P(t) = -\frac{2}{5}\int pvf_2(t, p)p^2 dp. \tag{A1}$$

In order to make sure we are capturing the main features of the ion and electron distribution functions shown in Figure 13 with this truncation, we calculate the ion and electron pressure anisotropies using Equation (A1) and the respective f_0 and f_2

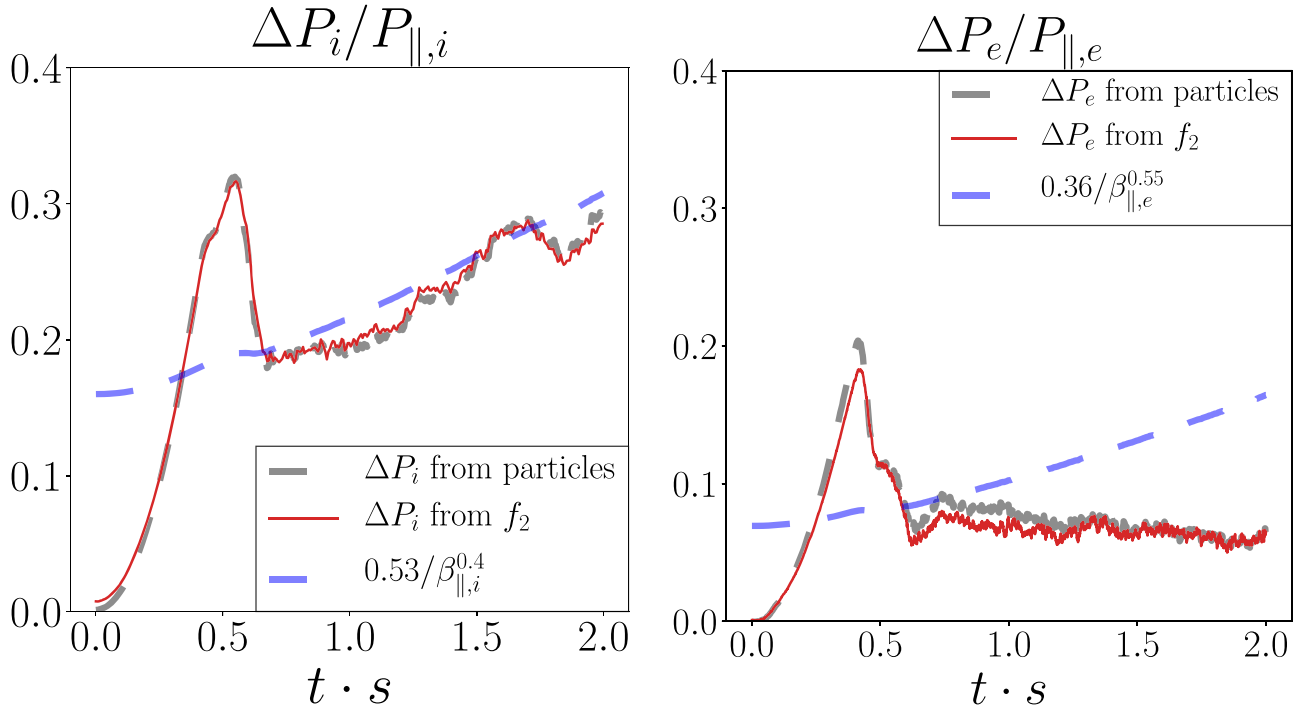

Figure 21. Left panel: the evolution of the ion pressure anisotropy for run b20m8w800. The gray-dashed line shows the anisotropy calculated averaging over the entire sample of ions (same as the green line shown in Figure 3(a)). The red line shows the ion anisotropy calculated from f_2 using Equation (A1). The blue-dashed line shows the IC threshold from Gary & Lee (1994). Right panel: the evolution of the electron pressure anisotropy for run b20m8w800. The gray-dashed line shows the anisotropy calculated averaging over the entire sample of electrons (same as the orange line shown in Figure 3(b)). The red line shows the electron anisotropy calculated from f_2 using Equation (A1). The blue-dashed line shows the whistler threshold from Gary & Wang (1996).

coefficients we obtained, shown in Figure 14. We can then compare with the pressure anisotropy shown in Figure 3, obtained directly by averaging over the same sample of 401,408 particles. This is shown in Figure 21.

We can see that the anisotropy recovered from f_0 and f_2 matches the particle-averaged anisotropy very well, so the majority of information about the distribution function is indeed contained in only the first two terms of the Legendre expansion.

ORCID iDs

Francisco Ley https://orcid.org/0000-0002-8820-8177
Ellen G. Zweibel https://orcid.org/0000-0003-4821-713X
Mario Riquelme https://orcid.org/0000-0003-2928-6412

References

Ahmadi, N., Wilder, F. D., Ergun, R. E., et al. 2018, JGRA, 123, 6383
Arzamasskiy, L., Kunz, M. W., Squire, J., Quataert, E., & Schekochihin, A. A. 2023, PhRvX, 13, 021014
Balbus, S. A. 2000, ApJ, 534, 420
Bale, S. D., Kasper, J. C., Howes, G. G., et al. 2009, PhRvL, 103, 211101
Baumjohann, W., Treumann, R. A., Georgescu, E., et al. 1999, AnGeo, 17, 1528
Berlok, T., Quataert, E., Pessah, M. E., & Pfrommer, C. 2021, MNRAS, 504, 3435
Bonafede, A., Feretti, L., Murgia, M., et al. 2010, A&A, 513, A30
Bott, A. F. A., Cowley, S. C., & Schekochihin, A. A. 2023, arXiv:2310.17754
Breuillard, H., Le Contel, O., Chust, T., et al. 2018, JGRA, 123, 93
Buneman, O. 1993, in Computer Space Plasma Physics: Simulation Techniques and Software, ed. H. Matsumoto & Y. Omura (Tokyo: Terra Scientific), 67
Chandrasekhar, S., Kaufman, A. N., & Watson, K. M. 1958, RSPSA, 245, 435
Chew, G. F., Goldberger, M. L., Low, F. E., & Chandrasekhar, S. 1956, RSPSA, 236, 112
Drake, J. F., Pfrommer, C., Reynolds, C. S., et al. 2021, ApJ, 923, 245
Gary, S. P. 1992, JGRA, 97, 8519
Gary, S. P., & Lee, M. A. 1994, JGRA, 99, 11297
Gary, S. P., & Wang, J. 1996, JGRA, 101, 10749
Giagkiozis, S., Wilson, L. B., Burch, J. L., et al. 2018, JGRA, 123, 5435
Hasegawa, A. 1969, PhFl, 12, 2642
Hellinger, P. 2007, PhPl, 14, 082105
Hitomi Collaboration, Aharonian, F., Akamatsu, H., et al. 2016, Natur, 535, 117
Jiang, W., Verscharen, D., Li, H., Wang, C., & Klein, K. G. 2022, ApJ, 935, 169
Jüttner, F. 1911, AnP, 339, 856
Kennel, C. F., & Engelmann, F. 1966, PhFl, 9, 2377
Kitamura, N., Omura, Y., Nakamura, S., et al. 2020, JGRA, 125, e2019JA027488
Kivelson, M. G., & Southwood, D. J. 1996, JGRA, 101, 17365
Komarov, S. V., Churazov, E. M., Kunz, M. W., & Schekochihin, A. A. 2016, MNRAS, 460, 467
Kunz, M. W., Schekochihin, A. A., Cowley, S. C., Binney, J. J., & Sanders, J. S. 2011, MNRAS, 410, 2446
Kunz, M. W., Schekochihin, A. A., & Stone, J. M. 2014, PhRvL, 112, 205003
Ley, F., Riquelme, M., Sironi, L., Verscharen, D., & Sandoval, A. 2019, ApJ, 880, 100
Ley, F., Zweibel, E. G., Riquelme, M., et al. 2023, ApJ, 947, 89
Melville, S., Schekochihin, A. A., & Kunz, M. W. 2016, MNRAS, 459, 2701
Perrone, L. M., & Latter, H. 2022a, MNRAS, 513, 4605
Perrone, L. M., & Latter, H. 2022b, MNRAS, 513, 4625
Píša, D., Sulaiman, A. H., Santolík, O., et al. 2018, GeoRL, 45, 486
Pokhotelov, O. A., Sagdeev, R. Z., Balikhin, M. A., & Treumann, R. A. 2004, JGRA, 109, A09213
Pokhotelov, O. A., Treumann, R. A., Sagdeev, R. Z., et al. 2002, JGRA, 107, 18
Riquelme, M. A., Quataert, E., Sharma, P., & Spitkovsky, A. 2012, ApJ, 755, 50
Riquelme, M. A., Quataert, E., & Verscharen, D. 2015, ApJ, 800, 27
Riquelme, M. A., Quataert, E., & Verscharen, D. 2016, ApJ, 824, 123
Roberg-Clark, G. T., Drake, J. F., Reynolds, C. S., & Swisdak, M. 2016, ApJL, 830, L9
Roberg-Clark, G. T., Drake, J. F., Reynolds, C. S., & Swisdak, M. 2018, PhRvL, 120, 035101

Rudakov, L. I., & Sagdeev, R. Z. 1961, SPhD, 6, 415
Schekochihin, A. A., & Cowley, S. C. 2006, PhPl, 13, 056501
Schekochihin, A. A., Cowley, S. C., Kulsrud, R. M., Hammett, G. W., & Sharma, P. 2005, ApJ, 629, 139
Schuecker, P., Finoguenov, A., Miniati, F., Böhringer, H., & Briel, U. G. 2004, A&A, 426, 387
Sironi, L., & Narayan, R. 2015, ApJ, 800, 88
Smith, E. J., Holzer, R. E., & Russell, C. T. 1969, JGR, 74, 3027
Southwood, D. J., & Kivelson, M. G. 1993, JGRA, 98, 9181
Spitkovsky, A. 2005, in AIP Conf. Proc. 801, Astrophysical Sources of High Energy Particles and Radiation 801 (Melville, NY: AIP), 345
Squire, J., Meyrand, R., Kunz, M. W., et al. 2022, NatAs, 6, 715
Stix, T. 1992, Waves in Plasmas (Melville, NY: AIP), 34
Towns, J., Cockerill, T., Dahan, M., et al. 2014, CSE, 16, 62
Tran, A., Sironi, L., Ley, F., Zweibel, E. G., & Riquelme, M. A. 2023, ApJ, 948, 130
Tsurutani, B. T., Smith, E. J., Anderson, R. R., et al. 1982, JGRA, 87, 6060
Zhang, H., Zhong, Z., Tang, R., et al. 2021, GeoRL, 48, e2021GL096056
Zhuravleva, I., Churazov, E., Schekochihin, A. A., et al. 2014, Natur, 515, 85
Zweibel, E. G. 2020, ApJ, 890, 67